

# DRIADA: A Python Toolkit for Cross-Scale Analysis of Single-Neuron Selectivity and Population Dynamics

Nikita Pospelov<sup>1,2\*</sup>, Viktor Plusnin<sup>1,2</sup>, Olga Rogozhnikova<sup>1,2</sup>, Anna Ivanova<sup>1,2</sup>, Vladimir Sotnikov<sup>3</sup>, Margarita Orobets<sup>1,4</sup>, Ksenia Toropova<sup>1,2</sup>, Olga Ivashkina<sup>1,2</sup>, Vladik Avetisov<sup>5</sup>, Konstantin Anokhin<sup>1,2</sup>

\*For correspondence:

[pospelov.na14@physics.msu.ru](mailto:pospelov.na14@physics.msu.ru) (NP)

<sup>1</sup>Institute for Advanced Brain Studies, Lomonosov Moscow State University, Moscow, Russia; <sup>2</sup>Moscow Physics and Technology Institute, Dolgoprudny, Russia; <sup>3</sup>Center for Interdisciplinary Research in Biology, Collège de France, Paris, France; <sup>4</sup>A.P. Nelyubin Institute of Pharmacy, I.M. Sechenov First Moscow State Medical University, Moscow, Russia; <sup>5</sup>Semenov Institute of Chemical Physics, Russian Academy of Sciences, Moscow, Russia

---

## Abstract

Brain activity spans single-neuron, population, and network levels, and core questions in neural coding require moving between them. Yet current tools target a single paradigm and incompatible data formats, leaving cross-level questions hard to address. We present DRIADA, an open-source Python framework that unifies neural signals and time-aligned behavior in a shared data model, so selectivity testing, dimensionality reduction, and network analysis operate within a unified workflow. We evaluate it on synthetic data with known ground truth, hippocampal calcium imaging from 13 mice in an open field, and a simulated toroidal attractor network. In the hippocampal data, selectivity-based filtering restored a two-dimensional spatial embedding from a collapsed all-neuron embedding, while reverse analysis showed that ~57% of neurons informative about leading manifold dimensions were not selective to any of the 11 measured behavioral features. On the toroidal benchmark, four independent modules recovered the expected topology. DRIADA makes cross-scale analysis routine across calcium imaging, spike trains, and simulated networks.

---

## Introduction

Single-neuron and population-level approaches provide complementary views of neural activity, but are rarely integrated within a common analytical framework. The tuning curves and selectivity profiles characterize how individual cells vary their activity in relation to experimentally defined sensory, spatial, or behavioral variables (*Hubel and Wiesel, 1962; O'Keefe and Dostrovsky, 1971*). At the population level, complementary approaches capture different aspects of collective organization: dimensionality reduction identifies the low-dimensional manifolds along which activity evolves (*Cunningham and Yu, 2014; Chung and Abbott, 2021*), while graph-theoretic analysis describes modular functional organization and its associations with behavior (*Bullmore and Sporns,*

2009; Sporns et al., 2005). In practice, however, each paradigm is typically pursued with its own tools, data formats, and conventions, so their integration requires combining unrelated codebases and translating between conceptual frameworks (Vaccari et al., 2022; Saxena and Cunningham, 2019).

Although these levels of analysis are conceptually distinct, their interplay is increasingly recognized as central to understanding neural coding. Some studies have linked them — for example, connecting single-neuron tuning to manifold structure (Chung and Abbott, 2021)—but cross-level studies remain rare, and the tooling gap mirrors the conceptual gap. Recent work argues that this fragmentation is not merely inconvenient but scientifically consequential. Munn et al. (2024) showed that the distinct coding signatures observed at different recording resolutions emerge from a common multi-scale organization of neural activity, indicating that scale-dependent theories of brain function describe different facets of a single underlying structure rather than fundamentally distinct phenomena. Vaccari et al. (2022) argued that population-level analyses remain incomplete without characterizing the individual neurons that compose the population. Dubreuil et al. (2022) using low-rank recurrent neural network (RNN) models demonstrated that the single-neuron subpopulation structure and the dimensionality of population dynamics play complementary roles in shaping network computations. Esparza et al. (2025) reported a parallel finding in the mouse hippocampus: cell-type specific subpopulations of CA1 neurons can exhibit distinct manifold geometries that are obscured when the entire hippocampal population is analyzed jointly. Together, these findings imply that the key questions in neural coding are inherently cross-level: Is single-neuron selectivity reflected in network membership? Does filtering by selectivity improve manifold reconstruction? Do all neurons identified as selective by single-neuron analysis contribute equally to population structure? Yet answering them with current tools demands custom pipelines that complicate analysis.

The need for integration is amplified by the scale and nature of modern recordings. Recordings now scale to populations of tens of thousands to a million neurons (Stringer et al. (2019); Manley et al. (2024)), while complex behavioral tasks rely on richer population codes (Rigotti et al., 2013; Fusi et al., 2016; Tye et al., 2024). Calcium imaging adds further constraints: it produces continuous fluorescence signals shaped by slow indicator kinetics (Climer and Dombeck, 2021). Together, these trends make a unified software workflow a practical prerequisite for cross-scale investigation.

Several packages address subsets of this analysis space, each operating within a single paradigm (Table 1).

**Information-theoretic toolboxes.** NIT (Maffulli et al., 2022) provides mutual information (MI) estimation, including Gaussian-copula mutual information (GCMI) for continuous signals and extensive bias corrections, but lacks autocorrelation-aware permutation testing, automatic variable type detection, or integration with dimensionality reduction and network analysis. MINT (Multivariate Information in Neuroscience Toolbox) (Lorenz et al., 2025) combines MI, partial information decomposition (PID), and feature-specific information transfer with dimensionality reduction in a MATLAB implementation. FRITES (Framework for Information Theoretical analysis of Electrophysiological data and Statistics) (Combrisson et al., 2022) offers GCMI-based MI workflows with group-level non-parametric permutation statistics for neurophysiological data. Information Dynamics Toolkit xl (IDTxI) (Wollstadt et al., 2019) and HOI (Neri et al., 2024) focus on information dynamics and higher-order interactions, respectively. To our knowledge, no existing package integrates single-neuron information testing, population manifold structure, and network analysis under a single Python data model.

**Spike-train and connectivity tools.** Elephant (Denker et al., 2024) (Electrophysiology Analysis Toolkit) provides spike-train statistics and connectivity estimation, but does not address population manifolds, single-neuron selectivity testing, or time-series-derived networks.

**Population-level tools.** CEBRA (Consistent EmBeddings of high-dimensional Recordings using Auxiliary variables) (Schneider et al., 2023) produces consistent embeddings through contrastive

**Table 1.** Feature comparison of DRIADA with related neural data analysis tools. Tools selected for inclusion provide at least one of: single-neuron MI testing, population dimensionality reduction, or functional network analysis. NIT ([Maffulli et al., 2022](#)) provides MI estimation; MINT ([Lorenz et al., 2025](#)) analyzes population-level information transmission; FRITES ([Combrisson et al., 2022](#)) provides MI-based neurophysiological statistics; CEBRA ([Schneider et al., 2023](#)) learns population embeddings; dPCA ([Kobak et al., 2016](#)) decomposes activity by task variable; Elephant ([Denker et al., 2024](#)) provides spike train statistics and connectivity estimation.

Feature	DRIADA	NIT	MINT	FRITES	CEBRA	dPCA	Elephant
Role of individual neurons	✓	✓	✓	—	—	✓	—
Autocorrelation-aware p-values	✓	—	—	✓	—	—	—
Diverse variable types	✓	✓	—	✓	✓	—	—
Population coding analysis	✓	—	✓	✓	✓	✓	✓
Network analysis	✓	—	—	✓	—	—	✓
Network analysis of time series	✓	—	—	—	—	—	—

learning and operates at the population level. CILDS (Calcium Imaging Linear Dynamical System) ([Koh et al., 2023](#)) jointly performs deconvolution and reduces dimensionality without selectivity analysis. Demixed PCA ([Kobak et al., 2016](#)) decomposes population activity by categorical task variable and provides encoder weights to quantify each neuron’s contribution to each component; its significance testing applies at the level of demixed components (via shuffling-based classification) rather than to individual neurons, and its scope is restricted to categorical task variables.

**Data frameworks.** Pynapple ([Viejo et al., 2023](#)) provides a typed time-series framework for neurophysiology with tuning curve computation and decoding, with scope limited to data manipulation and basic analyses. CalmAn ([Giovannucci et al., 2019](#)) handles upstream calcium imaging preprocessing and is complementary to DRIADA<sup>1</sup>, which begins where preprocessing ends.

An additional analytical dimension comes from complex systems science: constructing networks directly from individual time series ([Varley and Sporns, 2022](#)). Rather than preserving spatial information and collapsing time (as in functional connectivity), these methods preserve temporal structure, mapping a single neuron’s state-space trajectory into a graph. Recurrence networks capture how a signal revisits in phase-space using delay embedding ([Donner et al., 2010](#); [Marwan et al., 2007](#)); at the population level, pairwise similarity between per-neuron recurrence graphs yields functional networks based on temporal structure rather than activity covariance. Visibility graphs encode extreme-event structure without free parameters ([Lacasa et al., 2008](#); [Luque et al., 2009](#)), and ordinal partition networks quantify temporal complexity through symbolic dynamics ([Bandt and Pompe, 2002](#); [McCullough et al., 2015](#)). All three have been applied to neural data at the mesoscale—[Varley and Sporns \(2022\)](#) demonstrated all three on electrocorticography (ECoG) recordings—but applications at single-neuron resolution remain limited, with most reported uses in neuroscience concentrated at the electroencephalography / local field potential (EEG/LFP) scale ([Sulaimany and Safahi, 2023](#)). To our knowledge, no integrated package utilizes all three method families within a neuroscience-oriented workflow. Existing implementations either cover a single method (e.g., `ts2vg`<sup>2</sup> for visibility graphs) or span multiple methods but are developed primarily for climate and complex-systems applications (e.g., `pyunicorn` ([Donges et al., 2015](#))).

Each of these tools occupies a defined niche. The gap is not in any single analysis, but in the connections between them: there appears to be no existing Python package that integrates neuronal selectivity testing, manifold extraction, and network analysis within a single data model. Beyond this integration gap, the Python ecosystem for graph-analytic brain network analysis is also narrow: the Brain Connectivity Toolbox ([Rubinov and Sporns, 2010](#)) remains the reference implementation for graph metrics in neuroscience, but is MATLAB-based and operates on pre-constructed connectivity matrices, without tools for building networks from time series (visibility, recurrence, or

<sup>1</sup><https://github.com/iabs-neuro/driada>

<sup>2</sup><https://github.com/CarlosBergillos/ts2vg>

ordinal-partition graphs) or for integrating single-neuron and population-level analyses; its Python ports<sup>3</sup> have received little development in recent years.

DRIADA fills this gap with a shared data model that makes all analysis modules interoperable. Six modules operate on a common hierarchy of typed data objects: (1) single-neuron selectivity testing via GCMI (*Ince et al., 2017*) and Kraskov–Stögbauer–Grassberger (KSG) (*Kraskov et al., 2004*) estimators with autocorrelation-aware circular-shift permutation testing; (2) dimensionality reduction that spans linear, spectral, and autoencoder approaches (15 methods); (3) network analysis—functional connectivity, spectral decomposition, community detection, and thermodynamic entropy; (4) representational similarity analysis (*Kriegeskorte et al., 2008*); (5) information-theoretic utilities for custom MI and entropy computation; (6) network analysis of time series (recurrence networks, visibility graphs, ordinal partition networks) (*Varley and Sporns, 2022*). DRIADA implements all three time-series network methods alongside selectivity testing, dimensionality reduction, and network analysis; this paper demonstrates recurrence networks in a cross-scale workflow (Figure 5D).

A key design choice is that behavioral and environmental variables—sensory inputs, motor outputs, and internal states relevant to neural activity—are first-class objects in the same data model, stored as typed *TimeSeries* alongside the neural signals. As a result, selectivity testing, embedding analysis, and network construction all have native access to behavior without import or export steps. Variables undergo automatic type detection—continuous, discrete, circular, multivariate—so that appropriate estimators and preprocessing are selected automatically. Selectivity results can filter population matrices before dimensionality reduction; embedding coordinates become features for reverse selectivity analysis; graph-based dimensionality reduction returns proximity graphs that inherit the full network toolkit; multiple latent representations can be computed, compared, and linked back to individual neurons within a single experiment; and the same MI-based significance core underlies cell-variable, cell-cell, and variable-variable testing. Although this paper focuses on calcium imaging, the underlying data model is substrate-agnostic, processing calcium traces, spike trains, and artificial neural network activations through the same typed time-series abstraction. Rather than extending an existing toolbox, we implemented DRIADA from the ground up: integrating selectivity, population, and network analyses requires a shared underlying data model, which is not achievable through plugins to frameworks built around a single analytical layer.

We evaluated DRIADA through four increasingly complex demonstrations. We first validated the full pipeline on a synthetic population with known ground truth, then applied it to the hippocampal calcium imaging of 13 mice to test whether it recovers established selectivity profiles and to characterize the broader neuronal selectivity landscape of CA1. We then illustrated the cross-scale transitions that motivate the shared data model—using selectivity to reshape manifold geometry and using embedding coordinates to interrogate single-neuron roles. Finally, we simulated a toroidal continuous attractor network and asked whether four independent modules—selectivity testing, autoencoder embedding, representational similarity, and recurrence networks—converge on the same nonlinear topology.

## Results

### A unified data model for cross-scale neural analysis

DRIADA addresses the fragmented-toolchain problem described in the Introduction through a shared data model that makes all analysis modules interoperable (Figure 1). The six analysis modules are organized around complementary perspectives—single-neuron characterization, population-level geometry, and network structure—that form a triangle of cross-scale connections mediated by shared behavioral data (Figure 1A).

The *Experiment* object serves as the central container: it holds the neural activity matrix (raw

<sup>3</sup><https://github.com/aestrivex/bctpy>, <https://github.com/fiuneuro/brainconn>

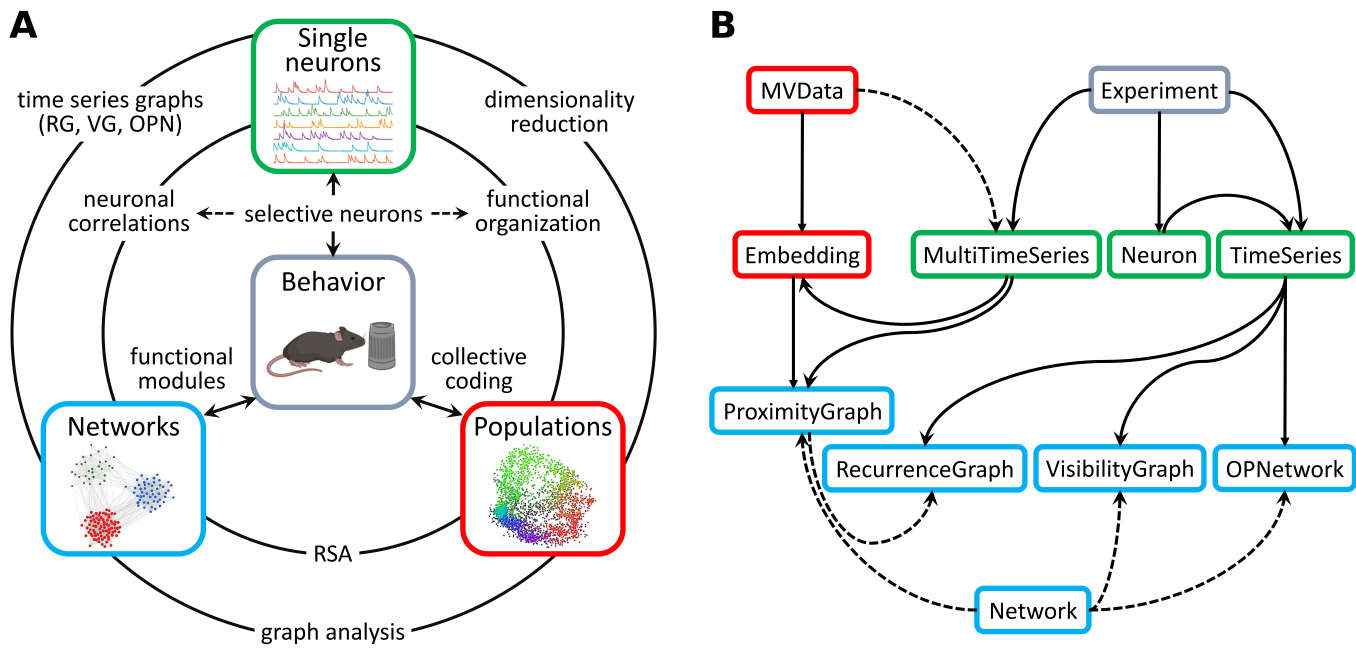


**Figure 1. DRIADA architecture and data model. (A)** Analysis workflow. Complementary perspectives—single-neuron characterization (green), population-level geometry (red), and network structure (blue)—form a triangle of cross-scale connections mediated by shared behavioral data (center). Outer arcs show analysis pathways that bridge scales: time series graphs (recurrence, visibility, ordinal partition) link single neurons to networks; dimensionality reduction links single neurons to populations; representational similarity analysis (RSA) and graph analysis link populations to networks. Inner arrows show behavioral anchoring: selectivity testing identifies individual neurons encoding specific behavioral variables; collective coding and functional modules connect behavior to population and network representations respectively. **(B)** Software object relationships. Each analysis perspective maps onto a set of interoperable Python classes. The *Experiment* container (gray) holds neural data as *MultiTimeSeries* and behavioral variables as *TimeSeries*; each *Neuron* stores its own traces (green). *MVDData* provides dimensionality reduction, producing an *Embedding* that contains a *ProximityGraph* (red). Single-neuron time series generate recurrence graphs, visibility graphs, and ordinal partition networks—all inheriting the full *Network* analysis toolkit (blue). Solid arrows indicate *produces* or *contains* relationships; dotted arrows indicate class inheritance.

calcium fluorescence or spike counts), time-aligned behavioral variables, and per-neuron meta-data in a single structure from which any module can draw without format conversion (Figure 1B). Each neuron’s activity is wrapped as a *TimeSeries*; the full population is jointly accessible as a *MultiTimeSeries* that inherits dimensionality-reduction capabilities from its parent class *MVDData*. Behavioral variables undergo automatic type detection upon loading: continuous features (e.g., position, speed), discrete features (e.g., object interaction, behavioral state), circular features (e.g., head direction), and multivariate features (e.g., two-dimensional coordinates) are classified and preprocessed appropriately—copula normalization for GCMI, integer coding for discrete entropy, and  $(\cos, \sin)$  encoding for circular variables. This automatic handling avoids a common source of errors: applying an inappropriate MI estimator to a misclassified variable.

**Single-neuron analysis** characterizes individual neurons from two complementary angles. Selectivity testing via INTENSE (Information-theoretic Neuron-feature Selectivity Testing; *Pospelov et al., 2026*), integrated into DRIADA) identifies *how* each neuron’s activity covaries with behavioral features—which variables it carries significant information about. Network analysis of time series characterizes *how* each neuron’s dynamics unfold: recurrence networks reveal dynamical macrostates via delay-embedded phase space topology; visibility graphs capture extreme-event structure and dynamical regime without free parameters; and ordinal partition networks quantify temporal complexity via permutation entropy. All three graph types inherit the full network analysis toolkit, so spectral decomposition, community detection, and entropy measures are immediately available on any single-neuron trace.

**Population activity analysis** compresses high-dimensional neural recordings into interpretable low-dimensional representations. Dimensionality reduction provides 15 methods spanning linear (PCA), spectral graph-based (Laplacian eigenmaps, diffusion maps, Isomap), neighborhood-based (t-SNE, UMAP), and neural network-based (autoencoder, variational autoencoder) approaches, plus intrinsic dimensionality estimators. Representational similarity analysis (RSA) compares neural representations across conditions via dissimilarity matrices and bootstrap significance testing.

**Network analysis** characterizes collective organization through functional connectivity, spectral decomposition, community detection, and thermodynamic entropy measures. The *Network* class provides a general-purpose graph-analysis framework that accepts sparse adjacency matrices or correlation matrices thresholded into edges.

These three perspectives are connected by six data-flow pathways (Figure 1A, arrows). From single neurons to populations, individual traces compose into a population matrix that feeds directly into any of 15 dimensionality reduction methods; selectivity results from INTENSE can filter the population before embedding, allowing direct comparison of full-population versus selective-population manifolds. From single neurons to networks, pairwise MI significance testing between neurons yields functional connectivity graphs, while per-neuron recurrence graphs, visibility graphs, and ordinal partition networks transform individual traces into graph representations whose pairwise similarity produces neuron–neuron networks that can be analyzed with the same community detection toolkit. From populations to networks, graph-based dimensionality reduction methods return a proximity graph that inherits the full network toolkit—spectral analysis, inverse participation ratio, entropy—so population manifold structure can be analyzed as a network without conversion; representational dissimilarity matrices provide a complementary route to the same network tools. A shared information-theoretic core (MI, conditional MI, entropy, time-delayed MI) underlies both the selectivity-testing and recurrence modules, providing a uniform statistical framework across scales.

### Recovering known structure from synthetic populations

To validate DRIADA's end-to-end pipeline, we generated a synthetic population with known ground-truth selectivity and modular network structure (see Methods). The population comprised two subpopulations: (i) 300 event-modulated neurons responding to three discrete behavioral events (E1, E2, E3): 180 single-event neurons (60 per event), 60 mixed-selectivity neurons responding to pairs of events (20 each for  $E1 \cup E2$ ,  $E1 \cup E3$ ,  $E2 \cup E3$ ), and 60 non-selective neurons; and (ii) 60 head-direction (HD) neurons with von Mises tuning ( $\kappa = 4.0$ ), along with 40 additional non-selective neurons. The full population of 400 neurons was simulated over 600 s at 20 Hz.

**Example selective neurons** (Figure 2A). Two representative neurons illustrate distinct selectivity types recovered by the pipeline. An event-selective neuron (left) shows elevated calcium transients during event epochs (green shading), with the corresponding density comparison (middle) confirming higher activity during on- versus off-periods. A head-direction-selective neuron (right) exhibits clear angular tuning in a polar plot of mean calcium activity as a function of head direction.

**Selectivity detection** (Figure 2B). The INTENSE pipeline was applied to the 300 event-modulated neurons across three discrete features. The MI heatmap shows mutual information values for all neuron–feature pairs, with significant pairs marked (black dots; two-stage test, 10,000 shuffles,  $p < 0.01$ , Holm correction). INTENSE correctly identified 300 significant pairs with  $F1 = 0.998$  (precision = 0.997, recall = 1.000), recovering the ground-truth modular selectivity structure including mixed-selectivity neurons. This benchmark uses idealized signal conditions (40x peak-to-baseline firing rate contrast, zero skip probability); sensitivity to noise and SNR is characterized in (Pospelov *et al.*, 2026).

**Manifold recovery** (Figure 2C). Isomap dimensionality reduction of the 60 HD-neuron subpopulation recovered the expected circular manifold. The two-dimensional embedding colored by ground-truth head direction angle shows a continuous ring topology, confirming that the population geometry preserves the circular behavioral variable. The circular–circular correlation between

embedding angle and ground-truth head direction was  $\rho_{\text{circ}} = 0.91$  (95% CI [0.90, 0.91]; circular-shift permutation test,  $p = 0.003$ , 1000 shifts), indicating strong preservation of angular relationships by the unsupervised nonlinear dimensionality reduction.

**Functional network and community detection** (Figure 2D–E). Cell–cell MI significance testing on the event-modulated subpopulation yielded a functional connectivity network with 10,158 significant edges among 300 neurons (edge density = 0.227). The giant connected component comprised 240 of 300 neurons; the 60 remaining isolates correspond to the non-selective subpopulation, which correctly received no significant inter-neuron connections. The spring-layout graph (panel D) is colored by six ground-truth neuron types: three pure-selectivity groups (E1, E2, E3) and three mixed-selectivity groups (E1∪E2, E1∪E3, E2∪E3). Mixed-selectivity neurons lie between the pure-selectivity clusters they bridge. Louvain community detection (resolution  $\gamma = 1.0$ , fixed random seed) recovered three communities corresponding to the three event types, plus 59 unclustered neurons closely matching the 60 planted non-selective units (adjusted Rand index, ARI = 0.721; normalized mutual information, NMI = 0.784). The imperfect agreement is structurally expected: mixed-selectivity neurons share significant connections with multiple event-type communities, making hard community assignment inherently ambiguous at community boundaries. The community-sorted adjacency matrix (panel E) shows within-community connections colored by their respective ground-truth group, with cross-community connections in gray. Block-diagonal structure shows that the detected communities align with the planted modular organization; off-diagonal connections near block boundaries correspond to mixed-selectivity neurons.

## Hippocampal selectivity landscape

After validating the pipeline on synthetic data with known ground truth, we next asked whether DRI-ADA could recover established biological findings from real hippocampal calcium imaging recordings and characterize the broader selectivity landscape of CA1. We applied the full pipeline to a dataset of 13 mice with one-photon miniscope recordings from dorsal CA1 during free exploration of a circular open-field arena (see Methods). For each session, we extracted 11 behavioral features, spanning continuous variables (two-dimensional position, head direction, body direction, speed) and discrete behavioral states (run, walk, rest, freezing, rearing, walls, center). We illustrate the pipeline on a representative session and report cross-animal statistics from 39 sessions across all 13 mice.

**Dataset overview and population embedding** (Figure 3A). The animal’s trajectory covered the arena broadly, with the occupancy heatmap confirming dense spatial sampling. To visualize population-level spatial structure, we applied UMAP to the calcium activity matrix of neurons identified by INTENSE as carrying significant information about position, wall-zone, or center-zone occupancy, and aligned the resulting two-dimensional embedding to the animal’s physical trajectory via Procrustes analysis (see Methods). The embedding preserves the spatial layout of the arena (Procrustes disparity = 0.40, where 0 indicates perfect correspondence and 1 no correspondence; vs.  $1.00 \pm 0.0003$  for permuted positions,  $p < 0.001$ , PROTEST with 999 permutations): points colored by two-dimensional position recapitulate the circular geometry of the open field. A control embedding computed from temporally shuffled calcium traces (independent circular shifts per neuron; see Methods) shows no spatial organization (disparity = 0.97), indicating that the observed manifold structure depends on intact temporal relationships in neural activity.

**Example selective neurons** (Figure 3B). Three representative neurons illustrate distinct selectivity types detected by INTENSE: a place cell with a spatially localized activity map; a head-direction cell with a clear angular tuning curve shown as a polar plot; and a locomotion-modulated cell whose calcium trace is elevated during locomotion epochs (orange shading), with the accompanying density plot confirming higher activity during locomotion versus rest.

**Selectivity prevalence across the population** (Figure 3C). To characterize the full selectivity landscape, we applied INTENSE to all 11 behavioral features across all 39 sessions and summarized the results using DRIADA’s cross-analysis database. For each mouse (averaging across sessions),

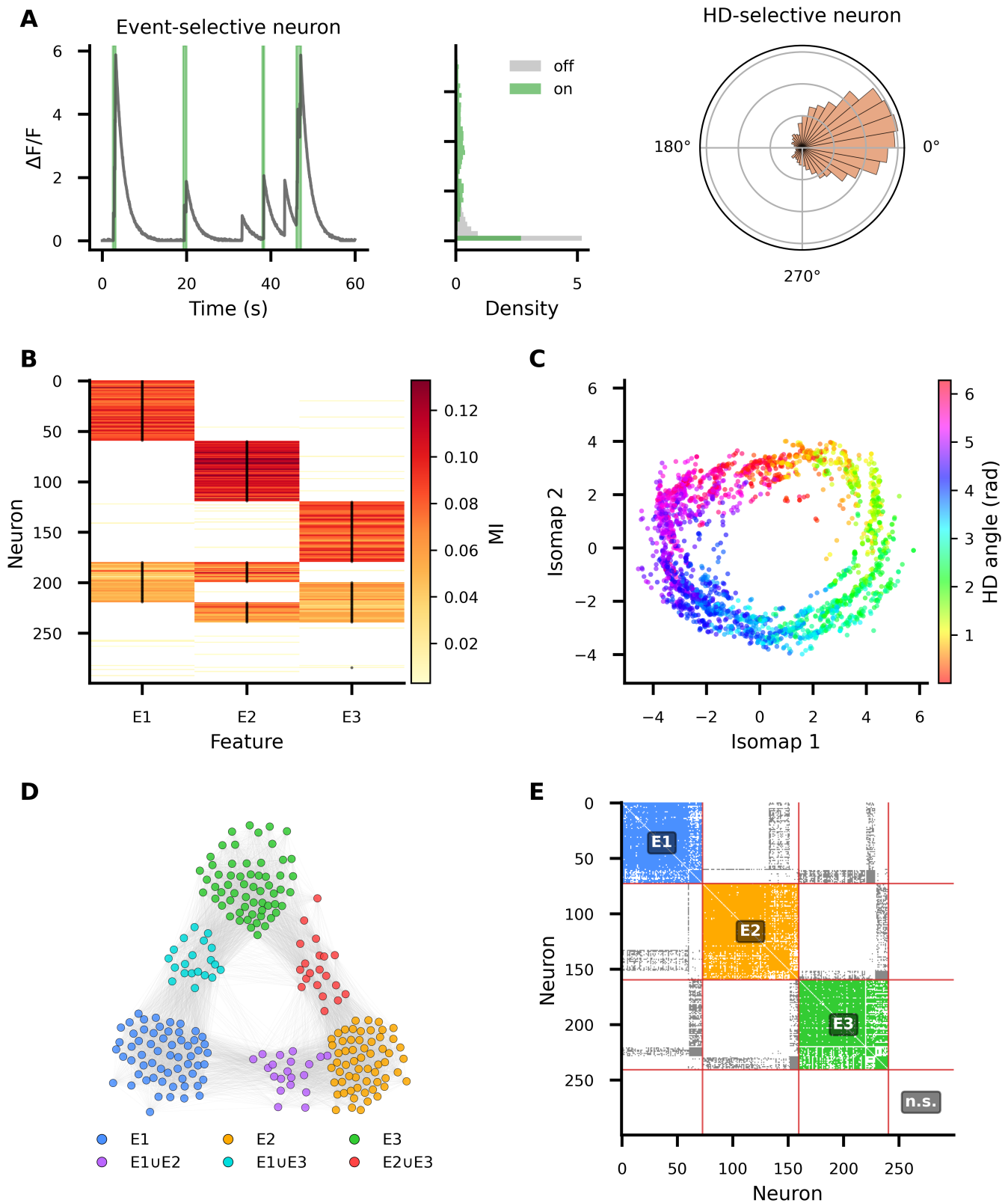


**Figure 2. End-to-end validation on synthetic data with known ground truth.** (A) Example selective neurons: an event-selective neuron (left) with calcium trace during event epochs (green) and corresponding density comparison (middle); a head-direction-selective neuron shown as a polar tuning curve (right). (B) MI selectivity heatmap for 300 event neurons across three discrete features (E1, E2, E3); significant pairs marked (F1 = 0.998). (C) Isomap embedding of 60 HD neurons colored by head direction angle, recovering the circular manifold. (D) Spring-layout network graph of event neurons colored by six ground-truth groups; mixed-selectivity neurons bridge pure-selectivity clusters. (E) Community-sorted adjacency matrix; within-community connections colored by neuron type, cross-community connections in gray (ARI = 0.721, NMI = 0.784).

we computed the percentage of neurons significantly selective to each feature (Figure 3C, left). Selectivity was widespread: five features (run, center-zone occupancy, walk, speed, and rest) had at least one significantly selective neuron in every animal, and the remaining six had it in 11–12 of 13 mice ( $p < 0.001$ ,  $MI > 0.04$ ; see (Pospelov et al., 2026) for threshold selection). The two mice lacking individual features had the lowest recording yields (~6–7 selective neurons per session), suggesting insufficient statistical power rather than absent coding. Overall, CA1 selectivity extends beyond the classically emphasized place and head-direction neurons to a rich, multidimensional behavioral space. Fast locomotion (run) selectivity was most prevalent (median 24.0% of selective neurons across mice, range 4–51%), followed by place (18.3%, 0–38%) and center-zone occupancy (13.5%, 6–23%). Head-direction selectivity (median 4.4%) was notably lower than typical proportions in head-direction-specialized regions Taube et al. (1990); Taube (1995), consistent with the well-documented but weaker HD modulation in dorsal CA1 Leutgeb et al. (2000); Acharya et al. (2016). Wall-zone selectivity was least prevalent (2.1%). This may reflect the operational definition of wall occupancy, occupancy distribution, or the fact that wall-related signals partly overlap with position and locomotion variables. The rank ordering of feature prevalences was significantly concordant across all 13 mice (Kendall's  $W = 0.53$ ,  $\chi^2 = 69.1$ ,  $p < 10^{-10}$ ), indicating a consistent—though not uniform—organizational property of CA1.

The accompanying bar chart (Figure 3C, right) shows the distribution of multi-feature selectivity. Of the selective neurons, 90.1% were selective exactly to one feature (95% confidence interval, CI: 87.7–92.4% across sessions), 9.3% to two features (7.0–11.6%), and 0.6% to three or more (0.3–1.0%). This predominantly single-feature profile likely represents a lower bound: the conservative significance threshold ( $p < 0.001$ ) reduces sensitivity to weak secondary associations, so neurons with additional, weaker tunings may be undercounted. Even so, the 9.9% of neurons selective to two or more features provide clear evidence of mixed selectivity (Rigotti et al., 2013; Fusi et al., 2016).

Taken together, these results demonstrate that DRIADA's integrated pipeline recovers well-established properties of hippocampal coding and characterizes the broader selectivity landscape of CA1 from a single dataset. Overall, 17.6% of neuron-sessions were classified as selective to at least one feature—a conservative estimate reflecting the strict significance threshold ( $p < 0.001$ ); published CA1 place cell fractions range widely depending on species, signal type, and detection criterion (Pospelov et al., 2026). The scale-bridging analysis below asks whether this selective minority accounts for population-level spatial structure, or whether the remaining nominally non-selective neurons also contribute.

### Scale-bridging: from selectivity to population structure and functional networks

A central design goal of DRIADA is to connect single-neuron selectivity with population-level and network-level structure. The shared data model makes these connections explicit: selectivity results can filter the population before dimensionality reduction, embedding coordinates can be treated as features for reverse selectivity analysis, and pairwise MI testing reveals functional connectivity. We demonstrate these cross-scale transitions on the same hippocampal dataset described above.

**Selectivity-filtered dimensionality reduction** (Figure 4A). We embedded the full population of 695 neurons and a filtered subset of 98 spatially selective neurons (identified by INTENSE as carrying significant information about position, wall-zone, or center-zone occupancy) via Isomap ( $k = 40$  neighbors, downsampled 5 $\times$ ) and Procrustes-aligned both embeddings to the animal's physical coordinates. Three spatial quality metrics quantify the effect of filtering (Figure 4A, right). The effective dimensionality ratio—variance along the minor axis relative to the major axis—increases from 0.11 (all neurons) to 0.80 (filtered), indicating that the all-neuron embedding collapses to a near-one-dimensional structure dominated by correlated activity variance, whereas the filtered embedding spans both arena dimensions. Position prediction ( $R^2 \approx 0.29$  for both embeddings) and pairwise distance correlation ( $\rho = 0.27$  all, 0.33 filtered) show that the linear spatial correspon-

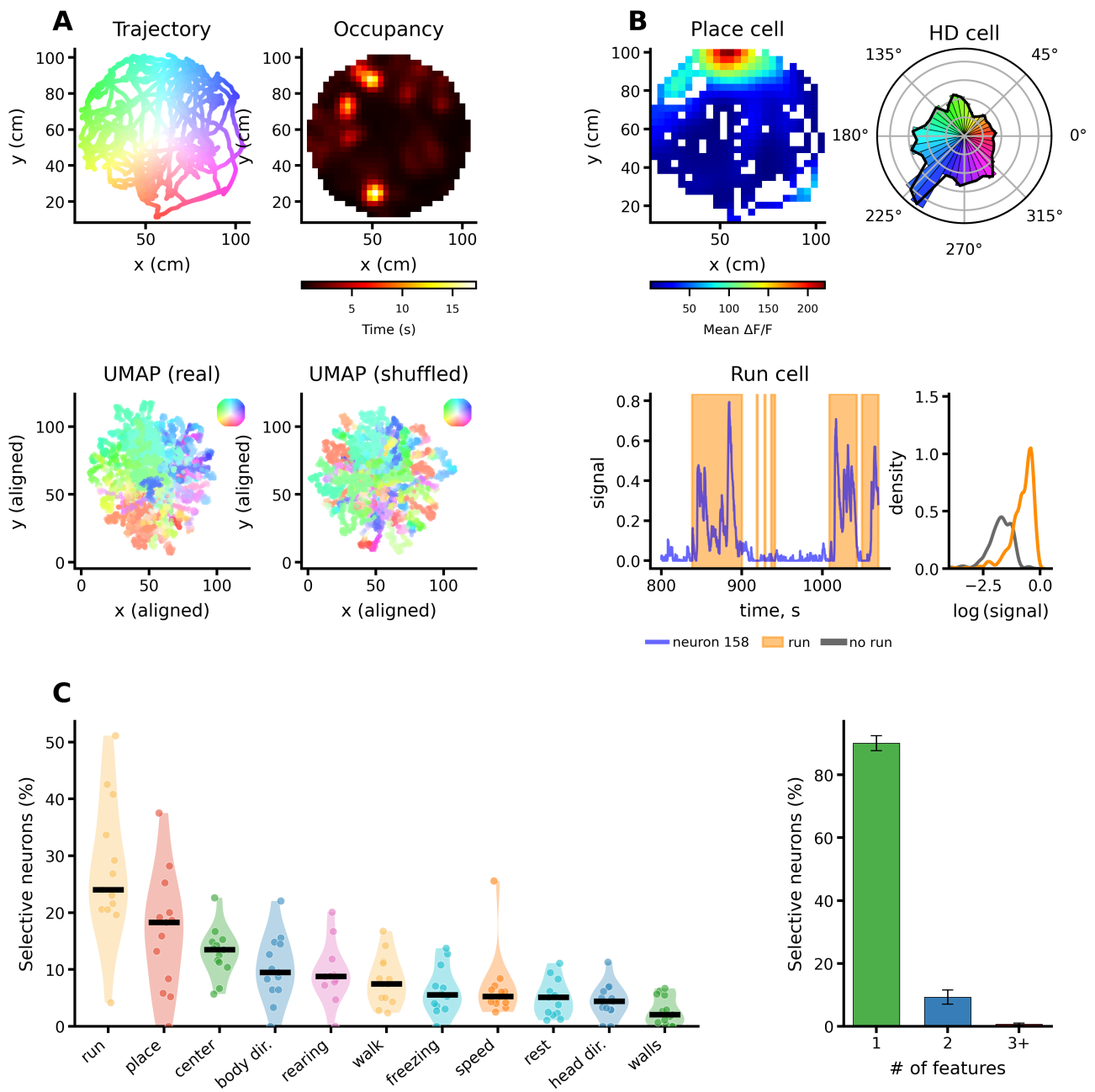


**Figure 3. DRIADA pipeline applied to hippocampal calcium imaging recordings during open-field exploration.** (A) Dataset overview for a representative session: animal trajectory colored by two-dimensional position (top left), spatial occupancy heatmap (top right), UMAP embedding of spatially selective neurons Procrustes-aligned to physical coordinates (bottom left), and the same embedding computed from temporally shuffled data (bottom right). (B) Example selective neurons: spatial calcium activity map of a place cell (top left), polar tuning curve of a head-direction cell (top right), and calcium trace overlaid with runs for a run-modulated cell (bottom left) with the corresponding activity-density comparison (bottom right). (C) Selectivity prevalence across 13 mice (left): violin plots show the percentage of neurons selective to each of 11 behavioral features, with individual mice as data points and median indicated by a horizontal bar. Bar chart (right): percentage of selective neurons selective to one, two, or three or more features (mean  $\pm$  95% CI across sessions).

dence is comparable, but the filtered embedding provides a two-dimensional manifold spanning the arena. Shuffled controls, in which each neuron’s calcium trace is shifted independently using circular shifts to destroy neuron–behavior coupling—abolish spatial correspondence across all three metrics ( $R^2 < 0.15$ ,  $\rho < 0.13$  for all-neuron shuffled;  $R^2 = 0.05$ ,  $\rho = 0.06$  for filtered shuffled). This indicates that the observed spatial structure reflects genuine neural encoding rather than single-cell statistics.

**Embedding selectivity analysis** (Figure 4B). DRIADA can identify which neurons are significantly informative about each embedding dimension by applying the same MI-based significance testing used for behavioral features. Of 695 neurons, 60 significantly encode Isomap dimension 1 and 67 encode dimension 2 ( $p < 0.05$ , two-stage test, 10,000 shuffles). Grouping these embedding-driving neurons by their primary INTENSE behavioral selectivity type shows a consistent functional composition: spatially selective neurons together account for a substantial share of the drivers, while ~57% (95% CI 51–63%) of manifold-informative neurons are classified as non-selective by INTENSE; because this fraction depends on the significance threshold used to define selectivity, we report it as a demonstration of the reverse-analysis capability rather than a fixed estimate. This analysis bridges scales in the reverse direction—from population structure back to individual neuron roles—and indicates that the spatial population manifold emerges from a mixture of overtly selective and nominally non-selective neurons.

**Functional network structure** (Figure 4C). We used DRIADA’s network module to construct a functional connectivity graph from pairwise cell–cell MI significance testing. The resulting network contains 678 neurons in the giant connected component with 3,517 significant edges. In the spring layout, each node is colored by its primary selectivity type. Neurons with similar selectivity form visually distinguishable clusters in the layout (e.g., place-selective, spatially selective, run-modulated), suggesting that functional connectivity in CA1 partially reflects shared feature tuning. A shuffled-data control network, constructed from temporally shifted traces, is substantially sparser (361 nodes, 392 edges) and shows no selectivity-based clustering. The normalized Laplacian spectral densities (Figure 4C, bottom) quantify this structural difference (Bobileva et al., 2025). In the real network, a cluster of small eigenvalues near zero—“soft” or “cluster” modes whose count corresponds to the number of weakly connected communities—is separated from a broad bulk, indicating well-defined modular organization; the absence of eigenvalues near 2 indicates the absence of bipartite substructures. In the shuffled network, no soft modes are separated from the bulk, indicating the absence of community structure; spectral density is concentrated near 1, a feature related to topologically equivalent nodes—neurons with indistinguishable connectivity patterns (Bobileva et al., 2025)—reflecting the homogeneous, unstructured topology; and spectral weight extends toward the bipartite limit near 2, a signature of sparse random graphs.

Taken together, these results illustrate DRIADA’s central design principle: the shared data model enables direct transitions between analysis scales. Selectivity testing (single neuron) filters and reshapes dimensionality reduction (population), embedding coordinates become features for reverse selectivity analysis, and pairwise MI significance testing yields functional connectivity aligned with selectivity types.

### Nonlinear manifold structure in a toroidal attractor network

To demonstrate DRIADA’s ability to recover nonlinear manifold structure, we simulated a 200-unit continuous attractor neural network (CANN) on a two-dimensional torus  $T^2 = S^1 \times S^1$  (see Methods). Each neuron was assigned a preferred position  $(\varphi_1, \varphi_2)$  on the torus with von Mises recurrent connectivity; two independent circular input variables  $\theta_1(t)$  and  $\theta_2(t)$  drove a localized activity bump across the network over 600 s at 20 Hz (Figure 5A). Toroidal CANNs are a standard model of grid cell population dynamics (Gardner et al., 2022) and have been proposed to underlie three-dimensional head-direction coding in bats, where azimuth and pitch jointly span a torus (Finkelstein et al., 2015). We used this system as a controlled benchmark because the underlying manifold topology is known exactly.

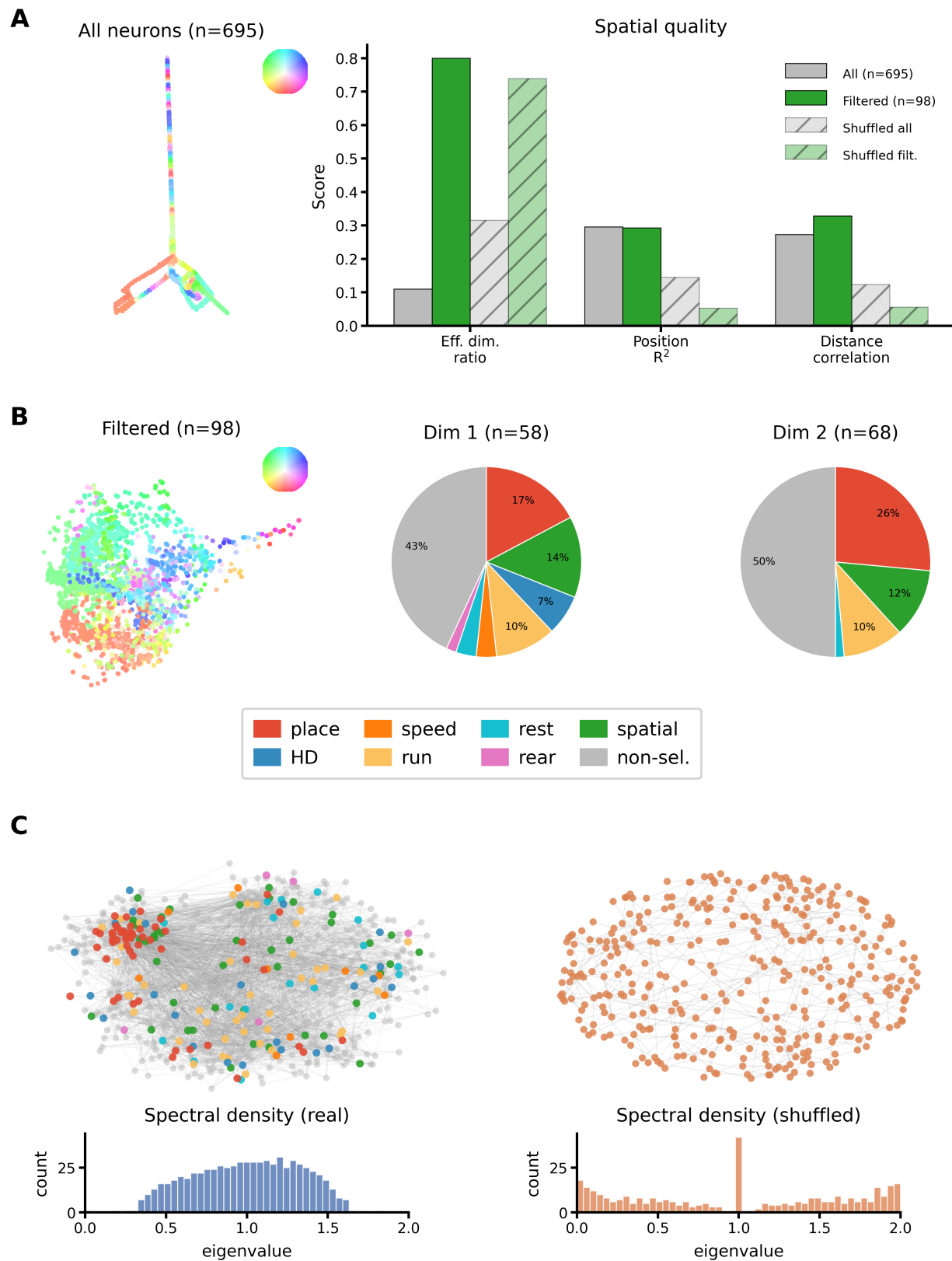


**Figure 4. Scale-bridging integration connects single-neuron selectivity to population structure and functional networks. (A)** Isomap embedding of all 695 neurons, Procrustes-aligned to physical coordinates and colored by two-dimensional arena position (left). Spatial quality metrics (right) compare all-neuron (gray), spatially filtered (green,  $n = 98$ ), and their respective shuffled controls (hatched): effective dimensionality ratio, position prediction  $R^2$ , and pairwise distance correlation  $\rho$ . **(B)** Filtered Isomap embedding ( $n = 98$  spatially selective neurons, left). Pie charts (right) show the behavioral selectivity composition of neurons significantly encoding each Isomap dimension (Dim 1:  $n = 60$ ; Dim 2:  $n = 67$ ), grouped by primary INTENSE selectivity type. **(C)** Functional network from cell-cell MI significance testing: real network (left, 678 nodes, 3,517 edges) with nodes colored by primary selectivity type, and shuffled control (right, 361 nodes, 392 edges). Bottom: normalized Laplacian spectral density histograms; the real network shows separated soft modes near zero (community structure) and a broad bulk, whereas the shuffled network shows no separated modes and spectral weight extending toward the bipartite limit near 2.

**Selectivity analysis** (Figure 5A). The INTENSE pipeline identified 152 neurons as significantly encoding  $\theta_1$  and 143 encoding  $\theta_2$  ( $p < 0.001$ , 10,000 shuffles) (95 were encoding both). All selective neurons carried significant information about both variables, consistent with the toroidal connectivity in which every neuron responds to a combination of the two inputs. However, per-neuron mutual information values revealed a continuous spectrum of relative encoding strength: 73 neurons were  $\theta_1$ -dominant (MI ratio  $> 0.6$ ), 72 were  $\theta_2$ -dominant ( $< 0.4$ ), and 55 were balanced, reflecting the diversity of preferred positions on the torus.

**Disentangling circular variables via autoencoder embeddings** (Figure 5B). The toroidal manifold poses a fundamental challenge for linear dimensionality reduction: each circular variable requires two linear coordinates ( $\cos \theta$ ,  $\sin \theta$ ) for faithful representation, so principal component analysis (PCA) with three components cannot capture both angles simultaneously (*Chung and Abbott, 2023*). We compared three-dimensional embeddings from PCA, a standard autoencoder (AE), and an autoencoder with a decorrelation loss (AE+corr) using the DCI (disentanglement, completeness, informativeness) score  $D$  (*Eastwood and Williams, 2018*), which measures whether each latent dimension encodes a single ground-truth variable ( $D = 1$ ) versus entangling multiple variables ( $D = 0$ ).

PCA achieved  $D = 0.27$ , reflecting the fundamental mismatch between linear coordinates and circular topology: each principal component partially correlates with both angles, as expected from the cos/sin projections. A standard autoencoder reached  $D = 0.87$  (best of 12 random initializations), showing that nonlinear dimensionality reduction can partially disentangle the two angles. Adding a decorrelation loss raised the ceiling to  $D = 0.96$  (best of 12 initializations): each latent dimension specialized to a single circular variable via nonlinear angle extraction (atan2), representing the full torus in three dimensions—two for the angles and one for bump amplitude.

**Representational similarity analysis** (Figure 5C). Condition-averaged population vectors were computed for nine conditions on the torus ( $3 \times 3$  grid of  $\theta_1$  and  $\theta_2$  positions). The resulting representational dissimilarity matrix (RDM; correlation distance) shows block-diagonal structure: conditions sharing a  $\theta_1$  or  $\theta_2$  value cluster together, providing a complementary, condition-level view of the same toroidal geometry recovered by the embedding analysis.

**Temporal dynamics via recurrence networks** (Figure 5D). Per-neuron recurrence graphs were constructed from delay-embedded activity traces (automatic embedding dimension and delay estimation;  $k$ -NN thresholding with  $k = 20$ ). We summarized each neuron by its own recurrence graph and linked neurons by the similarity between these graphs—a *network of networks*. Pairwise Jaccard similarity between recurrence graphs yielded a neuron–neuron functional network (141 neurons in the giant connected component, 2,975 edges after 85th-percentile thresholding of Jaccard similarities, chosen to retain the densest connections while preserving a connected graph). Spring-layout visualization of this network recovers spatial organization matching the ground-truth preferred-position plane ( $\varphi_1, \varphi_2$ ): pairwise Jaccard similarity between recurrence graphs correlated with toroidal proximity between neurons' preferred positions (Spearman  $\rho = 0.26$ ; significance assessed by a Mantel permutation test that respects the non-independence of neuron pairs,  $p < 10^{-4}$ , 10,000 permutations; see Methods). The modest effect size reflects that the thresholded recurrence-graph summary captures a real but partial signature of toroidal proximity; the recurrence-derived network nonetheless reflects the underlying toroidal geometry without access to stimulus variables.

Taken together, four DRIADA modules—selectivity testing, autoencoder-based dimensionality reduction, representational similarity analysis, and network analysis of time series—converge on the same toroidal structure from different analytical perspectives. Each module emphasized a different aspect of the underlying organization: selectivity testing identifies the continuous gradient of relative encoding strength across the population; the autoencoder disentangles the two circular variables that PCA cannot separate; RSA confirms block-diagonal condition-level geometry; and recurrence networks recover the spatial organization of the network from temporal dynamics alone, without access to the stimulus variables.

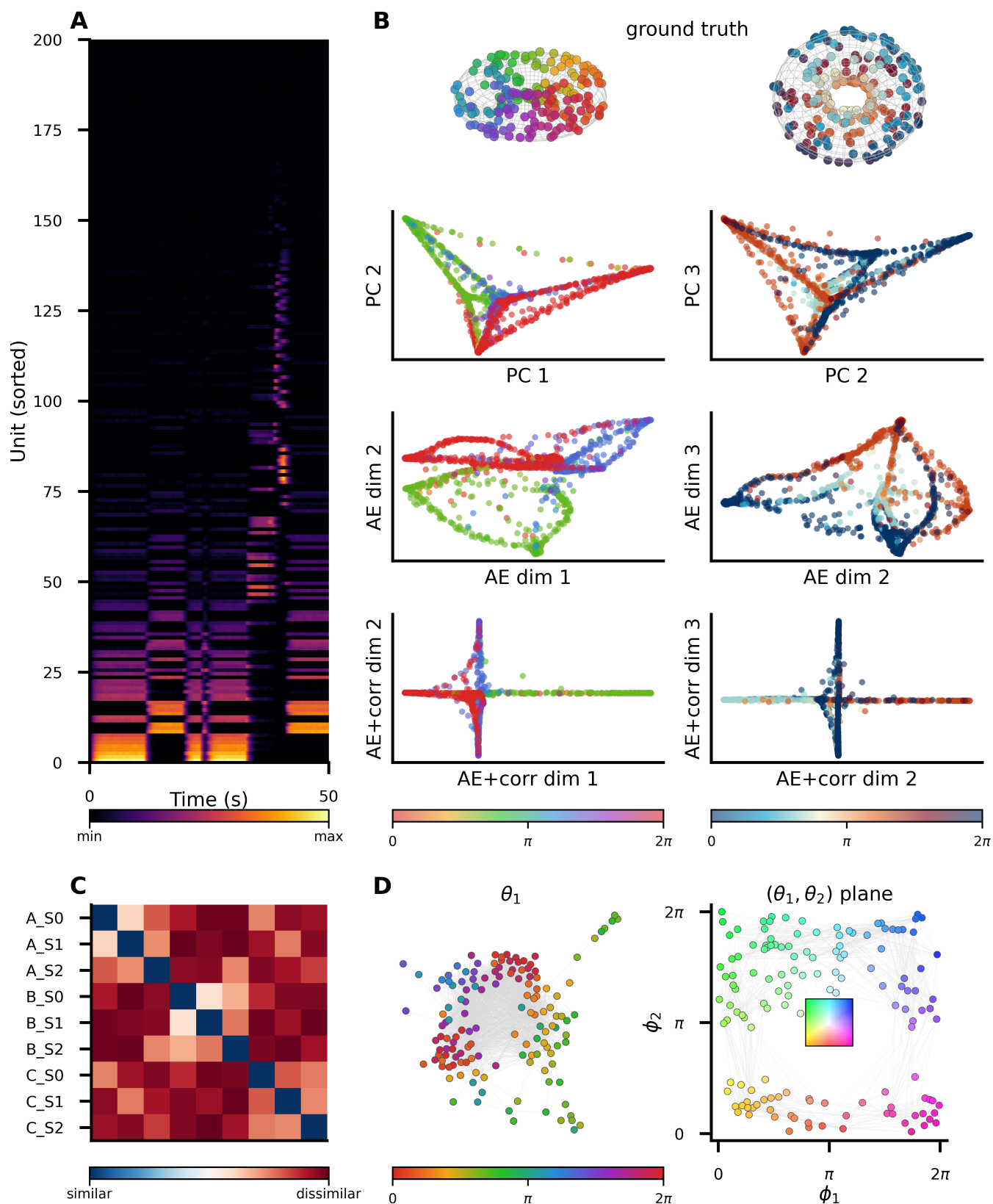


**Figure 5. Multiple DRIADA modules recover toroidal manifold structure in a continuous attractor network.** (A) Activity raster of a 200-unit CANN on  $T^2$  driven by two circular variables  $\theta_1$  and  $\theta_2$ . INTENSE identifies 152 and 143 neurons as significantly encoding each variable; all selective neurons are mixed-selective, with a continuous spectrum of relative encoding strength. (B) Three-dimensional embeddings colored by ground-truth  $\theta_1$  (left column) and  $\theta_2$  (right column). Ground-truth torus (top) shows neuron preferred positions. PCA ( $D = 0.27$ ) partially entangles the two circular variables; a standard AE ( $D = 0.87$ ; all AE scores best of 12 initializations) partially disentangles; an AE with decorrelation loss ( $D = 0.96$ ) achieves near-complete disentanglement. (C) Representational dissimilarity matrix for  $3 \times 3$  conditions on the torus, showing block-diagonal structure consistent with the toroidal geometry. (D) Network-of-networks analysis: per-neuron recurrence graphs combined via jaccard similarity. Spring layout (left) recovers spatial organization matching the ground-truth  $(\phi_1, \phi_2)$  plane (right).

## Discussion

The four demonstrations presented here show that a shared data model makes cross-scale analysis routine rather than bespoke. On synthetic data with known ground truth, the end-to-end pipeline recovered planted selectivity structure, circular manifold geometry, and modular network organization from the same population (Figure 2). On hippocampal calcium imaging recordings from 13 mice, DRIADA detected widespread selectivity across all 11 behavioral features and characterized the broader selectivity landscape of CA1, including a small but reliable fraction of multi-feature neurons (Figure 3). The scale-bridging analysis showed that selectivity-based filtering transforms a collapsed one-dimensional embedding into a two-dimensional spatial manifold, and that reverse selectivity analysis identifies the neurons contributing to each manifold dimension—including the ~57% (95% CI 51–63%) classified as non-selective by INTENSE (Figure 4). On a toroidal continuous attractor network, four modules—selectivity testing, autoencoder embedding, representational similarity analysis, and recurrence networks—independently converged on the same manifold topology (Figure 5). DRIADA additionally implements visibility graphs and ordinal partition networks, addressing a software gap identified by *Varley and Sporns (2022)*. We focused the present demonstrations on recurrence networks because they naturally connect to the population-level network-of-networks analysis. Individual modules have been applied in prior work to hippocampal place-cell dynamics (*Sotnikov et al., 2022*), population dimensionality estimation (*Pospelov et al., 2024*), fMRI resting-state analysis (*Pospelov et al., 2021*), structural connectome characterization (*Bobyleva et al., 2025*), and functional network entropy (*Pospelov et al., 2022*). DRIADA brings these methods into a single integrated framework.

The most striking cross-scale finding is that ~45% of neurons driving the spatial population manifold are classified as non-selective by INTENSE (Figure 4B). This observation reframes “non-selective” as a property of the statistical test and the chosen feature set rather than the neuron: these cells may carry sub-threshold spatial tuning too weak to reach significance in pairwise MI testing, or they may covary with latent variables not among the 11 measured features. *Stringer et al. (2019)* showed that population codes in visual cortex are inherently high-dimensional, suggesting that individual neuron selectivity is a poor predictor of population-level information content—our finding is consistent: neurons that do not individually pass a significance test nonetheless contribute collectively to the spatial manifold. The scale-bridging analysis illustrates the scale-dependent artifacts described by *Munn et al. (2024)*: the all-neuron embedding collapsed to a near-one-dimensional structure (dimensionality ratio 0.11), while selectivity-filtered embedding recovered the two-dimensional arena geometry (0.80)—a researcher using only population-level dimensionality reduction could draw substantially different conclusions about manifold structure. Our finding extends *Vaccari et al. (2022)* in both directions: not only does population analysis benefit from individual neuron characterization, but individual neuron characterization alone is incomplete, because nominally non-selective neurons contribute collectively to the spatial manifold.

Of neurons selective to at least one feature, 90.1% were selective to exactly one feature—a predominantly single-feature profile, in contrast to the strong mixed selectivity reported in prefrontal and association cortex (*Rigotti et al., 2013; Fusi et al., 2016*) (with the caveat that our conservative threshold may undercount weak secondary tunings). The rank ordering of feature prevalences was consistent across all 13 mice (Kendall’s  $W = 0.53$ ), indicating a systematic organizational property of CA1 despite substantial inter-animal variability in absolute prevalence. Cross-session analysis of CellReg-matched neurons reveals that selectivity labels are largely session-specific: only 1.1% of run-selective and 0.3% of place-selective neurons retained their label across all three sessions, though this retention was significantly enriched above chance. This is consistent with representational drift in CA1 (*Ziv et al., 2013; Geva et al., 2023*) and suggests that INTENSE detects selectivity that is statistically reliable within sessions but changes across days.

A design consequence of organizing all graph-based analyses around a single network representation is that spectral decomposition, community detection, and entropy measures apply uniformly

across scales. Functional connectivity graphs derived from cell–cell MI testing (Figure 4C), proximity graphs produced by graph-based dimensionality reduction (Laplacian eigenmaps, diffusion maps, Isomap), and per-neuron recurrence graphs (Figure 5D) all inherit the same analytical toolkit. This uniformity opens specific cross-scale comparisons—for example, testing whether communities detected in a functional connectivity network correspond to clusters in the embedding proximity graph, or whether spectral properties of recurrence networks predict population-level organization.

The normalized Laplacian spectral densities in Figure 4C illustrate this. In the real functional network, separated soft modes near zero reflect well-defined communities whose count corresponds to the number of weakly connected modules; the broad spectral bulk and the absence of eigenvalues near 2 indicates non-bipartite, heterogeneous topology. In the shuffled network, no soft modes separate from the bulk, spectral density concentrates near 1 (reflecting topologically equivalent nodes), and weight extends toward the bipartite limit—a signature of sparse random graphs. These spectral fingerprints distinguish structured from unstructured networks in a single summary, complementing the discrete community assignments from Louvain detection.

Recurrence networks preserve temporal structure that correlation-based functional connectivity collapses. From a dynamical systems perspective (*Vyas et al., 2020*), recurrence networks capture attractor geometry through delay embedding (*Donner et al., 2010*), making them sensitive to dynamical regime—a property not captured by correlation-based edges. The CANN benchmark (Figure 5D) demonstrates this concretely: recurrence-derived communities partially recover the toroidal organization from temporal dynamics alone, without access to stimulus variables.

All network analyses in DRIADA are pairwise. *Battiston et al. (2021)* argue that higher-order interactions involving groups of three or more units are pervasive in neural systems; the planned integration of partial information decomposition (*Williams and Beer, 2010*) would begin to address this limitation.

The hippocampal and CANN results both demonstrate that independent analytical perspectives converge on consistent structure when operating within a shared representation. In the hippocampal data, selectivity testing identifies spatially tuned neurons, population embedding recovers the arena geometry, and functional network analysis detects selectivity-aligned communities with modular spectral structure (Figures 3–4)—complementary analytical routes reaching the same conclusion. In the CANN, four modules converge on the same toroidal topology, illustrating the prediction of (*Dubreuil et al., 2022*) that connectivity shapes dynamics: the toroidal recurrent connectivity produces toroidal population dynamics, and each module independently recovers this correspondence. Together, these demonstrations illustrate the argument of *Munn et al. (2024)* that multi-scale analysis provides convergent evidence that recovered structure reflects underlying organization rather than method-dependent artifacts.

## Limitations

The default MI estimator (GCMI) provides a lower bound on mutual information via Gaussian copula transformation (*Ince et al., 2017*); for non-monotonic relationships it is therefore conservative rather than invalid. Because significance is determined by comparing the observed MI to a shuffled null distribution—not by its absolute magnitude—a neuron whose MI is underestimated can still be detected as significant whenever the true value exceeds the null, albeit with reduced statistical power. The alternative KSG estimator (*Kraskov et al., 2004*) captures arbitrary dependencies at higher computational cost; a systematic comparison of estimator choice on detection power is provided in (*Pospelov et al., 2026*).

The INTENSE pipeline includes an optional disentanglement stage using conditional MI and interaction information to separate genuine mixed selectivity from spurious associations caused by covarying behavioral variables; this stage is documented in the API but was not used in the demonstrations presented here.

Although the data model is substrate-agnostic—and has been applied to artificial recurrent neu-

ral networks (*Kononov et al., 2025*)—the selectivity-testing pipeline has been primarily validated on calcium imaging data. Temporal parameters (circular-shift edge masks, delay optimization window) are calibrated for the slow dynamics of calcium indicators; application to electrophysiology or LFP data may require adjustment of these defaults.

The pairwise cell–cell MI computation scales as  $O(N^2)$  in neuron count; for recordings exceeding  $\sim 5,000$  neurons, cell–cell significance testing may become a computational bottleneck. The neuron–feature pipeline (INTENSE) scales linearly in neuron count and completes in  $\sim 15$  seconds for  $500$  neurons  $\times$   $20$  features.

The toroidal CANN benchmark (Figure 5) validates the framework on a clean simulation with known topology; performance on noisy real data with unknown manifold structure will depend on recording quality and the choice of embedding method. All analyses operate in batch mode; online or streaming processing is not currently supported.

Planned extensions include integration of partial information decomposition methods (*Williams and Beer, 2010*) to characterize redundant and synergistic coding alongside the existing MI framework.

The demonstrations presented here show that selectivity predicts network membership (Figure 4C), that filtering by tuning improves manifold structure (Figure 4A), and that temporal dynamics recover the same topology as population geometry (Figure 5D)—each a cross-scale question that has until now demanded a bespoke pipeline. By providing a shared data model where such questions can be addressed through standard operations, DRIADA makes integrated cross-scale analysis accessible to experimentalists working with calcium imaging, spike trains, or simulated networks.

## Methods and Materials

### Unified data representation

All modules operate on a shared hierarchy of data objects that eliminates format conversion between analysis stages. The top-level container, `Experiment`, stores a calcium-activity matrix of shape  $(N_{\text{cells}}, N_{\text{frames}})$ , an optional spike matrix of equal shape, a dictionary of time-aligned behavioral variables (`dynamic_features`), time-invariant metadata (`static_features` such as frame rate and indicator kinetics), and per-neuron objects (`Neuron`). Each `Neuron` wraps its calcium and spike traces as `TimeSeries` objects; the full population is jointly accessible as a `MultiTimeSeries`, which inherits dimensionality-reduction capabilities from its parent class `MVData`.

`TimeSeries` is the fundamental univariate container. On construction, it runs automatic type detection (`analyze_time_series_type`) that classifies the signal as continuous (linear or circular) or discrete (binary, categorical, count, or timeline) and records the result as a `TimeSeriesType` object carrying subtype, confidence, and—for circular variables—period. The detection uses statistical heuristics (uniqueness ratio, integer checking, autocorrelation peak analysis) and can be overridden by the user via an explicit `ts_type` parameter. From this classification, `TimeSeries` lazily precomputes the representations needed by downstream estimators: copula-normalized values (`copula_normal_data`) for GCMI (*Ince et al., 2017*), integer-coded values (`int_data`) for discrete entropy, scaled values (`scdata`) for correlation, and a KD-tree (`get_kdtree`) for KSG (*Kraskov et al., 2004*). Shannon entropy values are cached per downsampling factor to avoid recomputation across modules.

`MultiTimeSeries` extends this pattern to multiple aligned series. It validates that all component `TimeSeries` share the same type and length, combines their shuffle masks via logical AND, and exposes joint entropy and copula-normalized matrices. Because `MultiTimeSeries` inherits from `MVData`, any neural population matrix can be reduced to a low-dimensional embedding via `get_embedding(metl dim)` without leaving the data model. Graph-based methods (Laplacian eigenmaps, diffusion maps, UMAP, Isomap) additionally return a `ProximityGraph` that inherits the full network-analysis toolkit (see Network analysis below), creating a natural bridge from dimensionality reduction to network

analysis.

When an `Experiment` is constructed, behavioral variables are automatically wrapped as typed `TimeSeries` with appropriate shuffle masks that exclude temporal boundaries (the outermost 2 s on each side for behavioral features, preventing edge artifacts during circular-shift permutation testing). For circular features such as head direction, the framework automatically constructs a two-dimensional  $(\cos, \sin)$  representation, enabling MI estimation that respects the circular topology. Multivariate features (e.g., two-dimensional position) are stored as `MultiTimeSeries`, and the same MI core handles them via multivariate estimators. This automatic variable handling means that a single call to the selectivity-testing pipeline processes all features regardless of type, with no manual configuration.

### Information-theoretic selectivity testing

DRIADA integrates the INTENSE algorithm ([Pospelov et al., 2026](#)) for detecting statistically significant neuron–feature associations. The central function `compute_cell_feat_significance()` tests every neuron–feature pair via a two-stage permutation procedure: an initial screen with 100 circular time shifts prunes clearly non-significant pairs, followed by a validation stage with 10 000 shifts that fits a zero-inflated gamma distribution to the null MI values and applies Holm–Bonferroni correction at  $\alpha = 0.01$  (FWER). For the hippocampal dataset presented here, significance was determined using a stricter per-pair threshold ( $p < 0.001$ ,  $MI > 0.04$ ) without FWER correction; threshold selection is discussed in ([Pospelov et al., 2026](#)).

Circular time-shift permutations—rather than naive shuffles—preserve the temporal autocorrelation of both calcium and behavioral signals, avoiding inflated false-positive rates. Because circular shifts correspond to circular cross-correlations, the convolution theorem computes MI at all  $n$  possible shifts in  $O(n \log n)$  rather than  $O(n_{sh} \cdot n)$  for  $n_{sh}$  individual shuffles, making large-scale permutation testing tractable. For a typical dataset of 500 neurons and 20 features, the full two-stage pipeline completes in approximately 15 seconds.

Two mutual-information estimators are available. The default, GCMi ([Ince et al., 2017](#)), transforms signals to Gaussian copula space and computes MI via a closed-form expression that integrates directly into the FFT pipeline; it captures monotonic nonlinearities and is well-suited for production-scale analysis. The KSG estimator ([Kraskov et al., 2004](#)) uses  $k$ -nearest-neighbor statistics and captures arbitrary nonlinear dependencies, including bell-shaped and ROI-based tuning, at higher computational cost. The estimator is selected automatically based on variable type but can be overridden by the user.

Delay optimization searches within a  $\pm 2$  s window (in 0.05 s steps) to account for GCaMP indicator kinetics and prospective or retrospective encoding. An optional disentanglement stage uses conditional MI and interaction information to separate genuine mixed selectivity from spurious associations caused by covarying behavioral variables. Full algorithmic details, including the zero-inflated gamma null model and the FFT acceleration scheme, are described in ([Pospelov et al., 2026](#)).

The same circular-shift MI framework extends to two additional testing modes. `compute_cell_cell_signifi` tests all neuron–neuron pairs rather than neuron–feature pairs, producing a binary significance matrix that serves as the adjacency matrix for functional connectivity networks (Figures 2D–E, 4C). `compute_embedding_selectivity()` treats embedding coordinates (e.g., Isomap or UMAP dimensions) as continuous features and applies the same two-stage permutation test to identify which neurons significantly encode each embedding dimension (Figure 4B). Both functions inherit the circular-shift permutation scheme, FFT acceleration, and multiple-comparison correction from the core pipeline.

Beyond significance testing, circular time shifts serve as a general control procedure throughout the pipeline. To generate a shuffled-data control for any downstream analysis (e.g., population embedding, functional network construction), each neuron’s calcium trace is independently circularly shifted by a random offset drawn uniformly from the interior of the recording (excluding

the outermost 1,000 frames on each side to avoid edge artifacts). This preserves each neuron's temporal autocorrelation and amplitude distribution while destroying inter-neuron temporal relationships and neuron-behavior coupling. Any structure that appears in the real data but vanishes in the shuffled control can therefore be attributed to coordinated neural dynamics rather than to single-cell statistics.

## Dimensionality reduction

The dimensionality-reduction module provides 15 methods accessible through a unified interface (`MVData.get_embedding(method, dim)`). Methods span four families: linear (PCA), spectral graph-based (Laplacian eigenmaps, diffusion maps (Coifman and Lafon, 2006), Isomap, locally linear embedding, Hessian LLE, maximum variance unfolding), distance-based (MDS), neighborhood-based (t-SNE, UMAP (McInnes et al., 2018)), and neural network-based (autoencoder, variational autoencoder, and a user-configurable flexible autoencoder). Spectral variants with automatic bandwidth selection (`auto_le`, `auto_dmaps`) are available for Laplacian eigenmaps and diffusion maps. All methods return an `Embedding` object that stores coordinates, the fitted model, and—for graph-based methods—a `ProximityGraph` inheriting the full network-analysis toolkit (see Network analysis below).

Because neural activity matrices are stored as `MultiTimeSeries`, which inherits from `MVData`, population data can be embedded directly. Graph-based methods first construct a  $k$ -nearest-neighbor proximity graph (default  $k = 15$ ,  $L_2$  metric) and then solve an eigenvalue problem on the graph Laplacian; the resulting graph is retained so that subsequent spectral and community analyses can be performed without graph reconstruction. Sequential reduction pipelines (e.g., PCA to 50 dimensions followed by UMAP to 2 dimensions) are supported through `dr_sequence()`.

Embedding quality is assessed by several complementary metrics: `trustworthiness` and `continuity` (Venna and Kaski, 2006) measure how well the embedding preserves local neighborhoods; `k`-nearest-neighbor preservation rate (`knn_preservation_rate`) quantifies the fraction of neighbors retained; and `geodesic distance correlation` evaluates global structure preservation. For neural network methods, reconstruction error and latent-space metrics are reported automatically. Procrustes analysis (`procrustes_analysis`) aligns a target embedding to a reference coordinate system via rotation and, optionally, scaling and reflection, enabling direct visual comparison between neural manifolds and behavioral variables such as spatial position. When external reference coordinates are available (e.g., the animal's physical position), three additional metrics assess spatial fidelity: the *effective dimensionality ratio* (variance along the minor embedding axis divided by variance along the major axis; 0 = collapsed to one dimension, 1 = isotropic), the *position  $R^2$*  (multivariate linear regression from embedding coordinates to reference position), and the *pairwise distance correlation* (Spearman  $\rho$  between pairwise distances in embedding space and reference space, subsampled to 2,000 points for tractability).

The dimensionality-estimation module complements reduction with tools for determining intrinsic dimensionality: PCA-based thresholding (fraction of variance explained), effective rank (spectral entropy of eigenvalues),  $k$ -nearest-neighbor dimension, correlation dimension (Grassberger-Procaccia), and geodesic dimension (Jazayeri and Ostojic, 2021). These estimators inform the choice of target dimensionality for reduction.

## Network analysis

The `Network` class provides a general-purpose graph-analysis framework that underlies both functional connectivity analysis and the proximity graphs produced by graph-based dimensionality reduction. A `Network` can be constructed from a sparse adjacency matrix, a `NetworkX` graph, or from a pairwise correlation matrix thresholded into binary edges. Directed, undirected, weighted, and unweighted graphs are supported; directedness and weights are auto-detected from the adjacency structure when not specified explicitly.

Spectral decomposition is central to the analysis. The class computes eigenvalues and eigenvectors of the adjacency matrix, graph Laplacian, normalized Laplacian, random-walk Laplacian, or transition matrix on demand. From the spectrum, several summary statistics are derived: the inverse participation ratio (IPR) of each eigenvector quantifies its localization; free entropy, Rényi  $q$ -entropy, and spectral entropy characterize the graph's thermodynamic properties at user-specified diffusion times; and the Estrada communicability index measures global connectivity. Gromov hyperbolicity estimates characterize the global geometry of the graph. Degree-preserving randomization generates null models for statistical comparison. Community detection is provided via the Louvain algorithm (with configurable resolution parameter) through the NetworkX interface. Graph preprocessing options include extraction of the giant connected or strongly connected component and removal of self-loops and isolated nodes.

Because ProximityGraph (used by graph-based DR methods) inherits from Network, any embedding that produces a proximity graph—Laplacian eigenmaps, diffusion maps, Isomap, UMAP—automatically exposes the full spectral and community analysis toolkit. This inheritance creates a natural bridge between dimensionality reduction and network analysis without additional code.

Representational similarity analysis (RSA) (Kriegeskorte *et al.*, 2008) is provided by a dedicated module. `compute_rdm()` constructs representational dissimilarity matrices from neural activity patterns using correlation, Euclidean, cosine, or Manhattan distance. Multiple entry points support different experimental designs: condition-averaged patterns, trial-level patterns, or labeled time series. RDMs are compared via Spearman or Pearson correlation, with significance assessed by bootstrap resampling (`bootstrap_rdm_comparison`).

## Network analysis of time series

Three complementary methods for constructing networks directly from time series (Varley and Sporns, 2022) are implemented as subclasses of Network, inheriting the full spectral and community analysis toolkit.

**Recurrence networks** (Donner *et al.*, 2010; Marwan *et al.*, 2007). A univariate time series is first embedded in a reconstructed phase space via Takens time-delay embedding (`takens_embedding`), with embedding dimension  $m$  and delay  $\tau$  estimated automatically via false nearest neighbors (Kennel *et al.*, 1992) and the first minimum of time-delayed mutual information, respectively. Pairs of embedded state vectors closer than a threshold (either  $\epsilon$ -ball or  $k$ -nearest neighbors) are connected by an edge; a Theiler window removes trivially correlated temporal neighbors. Recurrence quantification analysis (`compute_rqa`) extracts determinism, laminarity, trapping time, and diagonal-line entropy from the recurrence matrix. Community detection on the recurrence network identifies dynamical macro-states. At the population level, per-neuron recurrence matrices are combined into a joint recurrence plot (JRP) via thresholded element-wise intersection, and pairwise Jaccard similarity between individual matrices yields a neuron–neuron network amenable to further community analysis.

**Visibility graphs** (Lacasa *et al.*, 2008; Luque *et al.*, 2009). Two time points are connected if no intermediate value obstructs the “line of sight” between them. The horizontal visibility graph (HVG) uses an  $O(N)$  monotone-stack algorithm and requires no free parameters; the natural visibility graph (NVG) uses an  $O(N^2)$  pairwise check and captures additional geometric structure. The degree distribution of the resulting graph reflects the dynamical regime: fractal processes produce scale-free distributions, while uncorrelated random processes yield exponential distributions. Hub nodes correspond to extreme events in the original signal.

**Ordinal partition networks** (Bandt and Pompe, 2002; McCullough *et al.*, 2015). The time series is embedded via Takens delay embedding and each state vector is reduced to its rank-order pattern (ordinal pattern), encoded as a Lehmer code (an integer in  $[0, d!)$ , where  $d$  is the embedding dimension). Nodes of the network represent unique ordinal patterns; directed weighted edges encode transition probabilities between consecutive patterns (row-normalized, self-loops removed). Permutation entropy (the normalized Shannon entropy of pattern visit frequencies) summarizes

the complexity of the dynamics on a  $[0, 1]$  scale. Missing patterns indicate forbidden ordinal transitions.

All three graph types are accessible through the TimeSeries API (`ts.recurrence_graph()`, `ts.visibility_graph()`, `ts.ordinal_partition_network()`) with automatic parameter estimation and result caching.

### Synthetic data generation

DRIADA includes synthetic data generators that produce populations of neurons with known selectivity profiles, enabling quantitative validation of the full analysis pipeline. The canonical generator (`generate_tuned_selectivity_exp`) takes a declarative population specification: each neuron group is defined by its count, the features it responds to, and the tuning curve type—von Mises for head-direction selectivity, two-dimensional Gaussian for place fields, sigmoid for speed tuning, and threshold activation for discrete events. Multiple selectivity can be specified via OR (responsive to any feature) or AND (responsive only when all features are active) combination modes.

Behavioral variables are generated as correlated random processes: continuous features use fractional Brownian motion (fBM) with a configurable Hurst exponent  $H$  (default  $H = 0.3$ , producing anti-persistent trajectories with naturalistic episode structure); two-dimensional position follows a momentum-driven random walk with boundary reflection; circular variables (head direction) follow a circular random walk; and discrete events are generated as binary time series with configurable active fraction and average episode duration.

Neural responses are converted to realistic calcium fluorescence traces by convolving spike trains (generated via an inhomogeneous Poisson process with tuning-modulated rates) with a double-exponential kernel that models GCaMP6-like rise and decay dynamics ( $\tau_{\text{rise}} = 0.05$  s,  $\tau_{\text{decay}} = 2.0$  s). Additive Gaussian noise, random event amplitudes, and a configurable skip probability (probability of failing to respond during an active period) allow systematic control of the signal-to-noise ratio.

The generator returns a standard `Experiment` object with embedded ground truth—expected neuron–feature pairs, neuron type labels, and tuning parameters—so that detection rates (TPR, FPR, F1) can be computed directly against the known selectivity structure.

### Continuous attractor network simulation

The toroidal CANN benchmark (Figure 5) simulates a rate-model network of  $N = 200$  units on a two-dimensional torus  $T^2 = S^1 \times S^1$ . Each neuron  $i$  is assigned a uniformly random preferred position  $(\varphi_1^{(i)}, \varphi_2^{(i)}) \in [0, 2\pi)^2$ . The membrane potential evolves as

$$\tau \frac{dr_i}{dt} = -r_i + \left[ \sum_j W_{ij} r_j + I_{\text{ext},i}(t) + \eta_i(t) \right]_+ \quad (1)$$

with time constant  $\tau = 0.2$  s, ReLU activation  $[\cdot]_+ = \max(\cdot, 0)$ , and Gaussian noise  $\eta \sim \mathcal{N}(0, 0.05^2)$ . Recurrent weights follow a translation-invariant von Mises profile with global inhibition:

$$W_{ij} = \frac{J_{\text{exc}}}{N} \exp\left(\kappa_c (\cos(\varphi_1^{(i)} - \varphi_1^{(j)}) + \cos(\varphi_2^{(i)} - \varphi_2^{(j)}) - 2)\right) - \frac{J_{\text{inh}}}{N} \quad (2)$$

with  $J_{\text{exc}} = 8$ ,  $J_{\text{inh}} = 0.8$ , and connectivity concentration  $\kappa_c = 2.0$ . External input positions a bump at  $(\theta_1(t), \theta_2(t))$  via  $I_{\text{ext},i} = \exp(\kappa_{\text{in}} (\cos(\theta_1 - \varphi_1^{(i)}) + \cos(\theta_2 - \varphi_2^{(i)}) - 2))$  with input sharpness  $\kappa_{\text{in}} = 4.0$ .

Two independent circular latent variables  $\theta_1(t)$  and  $\theta_2(t)$  are generated as switching processes: each jumps between three equally-spaced positions on  $[0, 2\pi)$  with exponentially distributed dwell times (mean 10 s and 6 s respectively) and smooth transitions ( $\tau_{\text{tr}} = 0.3$  s). The simulation runs for 600 s at 20 Hz (12,000 frames). Raw firing rates are exponentially smoothed ( $\tau_{\text{smooth}} = 0.5$  s) and corrupted with additive observation noise ( $\sigma_{\text{obs}} = 0.01$ ) to mimic calcium indicator dynamics.

For disentanglement analysis, three-dimensional embeddings were computed via PCA and two autoencoder variants. The autoencoder architecture consists of a single hidden layer (128 units, ReLU) with a 3-dimensional bottleneck. The standard AE minimizes reconstruction error only (MSE

loss); the decorrelating variant adds a pairwise correlation penalty on the latent dimensions (weight 1.0). Both are trained for 200 epochs (Adam,  $\text{lr} = 10^{-3}$ , batch size 512). To account for sensitivity to initialization, each autoencoder is trained with 12 random seeds and the best DCI score is reported. Disentanglement is quantified by the DCI score (*Eastwood and Williams, 2018*): for each latent dimension, the importance weights (circular-linear  $R^2$ ) across ground-truth variables are normalized to a probability distribution, and  $D = 1 - \bar{H} / \log K$ , where  $\bar{H}$  is the mean entropy across dimensions and  $K = 2$  is the number of ground-truth variables.  $D = 1$  indicates each dimension encodes exactly one variable;  $D = 0$  indicates maximal entanglement.

For RSA, nine conditions were defined by crossing the three  $\theta_1$  positions with the three  $\theta_2$  positions; the representational dissimilarity matrix was computed from condition-averaged population vectors using correlation distance.

## Hippocampal calcium imaging dataset

### Animals

We used C57BL/6J mice (both sexes,  $n = 14$ ), aged 10–11 months. Before surgery, animals were housed in standard laboratory cages (2–7 per cage) under a 12-hour light/dark cycle, with free access to food and water. After surgery mice were housed individually; other housing conditions remained unchanged. All experiments were performed during the light phase of the day (10:00 a.m. to 6:00 p.m.). One animal was excluded due to insufficient signal quality, leaving 13 mice in the final analysis.

### Surgeries and viral delivery

All procedures were approved by the Commission of Bioethics of Lomonosov Moscow State University (Application № 159-g, approved during Bioethics Commission meeting № 154-d-r held on 17.08.2023), and followed the Russian Federation Order N 267 MZ and the NIH Guide for the Care and Use of Laboratory Animals.

Surgical procedures were carried out in three stages: viral injection, GRIN lens implantation, and baseplate installation. Anesthesia was induced by intraperitoneal injection of zoletil (40 mg/kg) and xylazine (5 mg/kg). Dexamethasone (4 mg/kg) was administered subcutaneously 5 minutes before surgery to reduce inflammation and prevent cerebral edema. Moisturizing gel was applied to prevent eye drying. Mice were positioned in a stereotaxic frame (Kopf, USA), and body temperature was maintained with a heated pad (Physitemp, USA). For virus injection, 300 nL of AAV1.CAG.GCaMP6s was delivered unilaterally into the dorsal CA1 region (coordinates: AP  $-1.94$  mm, ML  $+1.46$  mm, DV  $-1.2$  mm; *Paxinos and Franklin (2019)*). One week later, a 1-mm-diameter GRIN lens (GrinTech, Germany) was implanted 200  $\mu\text{m}$  above CA1. The lens was attached to the skull with cyanoacrylate glue (Henkel, Germany) and dental cement (Stoelting, USA), and covered with Kwik-Sil (World Precision Instruments, USA). One week after lens implantation, an aluminum baseplate was placed over the implant site for miniscope mounting and secured to the skull with dental cement. A removable plastic cap was placed over the implant to protect the lens. Following the final surgery, mice were returned to their home cages to recover.

### Behavioral procedure

Two weeks after the final surgery, mice were gradually habituated to handling and wearing a miniscope. For three consecutive days, each mouse was placed in its home cage with a connected but non-recording miniscope for 5 minutes per session. On the following three days, animals were tested in a circular open field arena (diameter 96 cm) with visual landmarks placed on the surrounding walls. Each session lasted approximately 12 minutes with 30 frames per second. Throughout each trial, animal behavior was recorded using a top-mounted video camera (Flir Chameleon3, KVR, UK), while CA1 calcium activity was simultaneously acquired via the miniscope (Miniscope V4.4). Behavioral video and miniscope streams were synchronized in Bonsai (Bonsai Foundation, UK) using shared timestamps, yielding aligned time bases for delay-dependent analyses.

## Behavioral analysis

Behavioral tracking and annotation were performed using the Sphynx package for exploratory behavior analysis (*Plusnin et al., 2024*). For each video, the positions of key body parts were estimated frame-by-frame using a DeepLabCut-trained neural network (*Mathis et al., 2018*). Coordinates with confidence scores below 0.95 were excluded and reconstructed by piecewise cubic interpolation using neighboring high-confidence frames. The resulting trajectories were smoothed with a third-degree Savitzky–Golay filter, applied with a 0.25-second window for the body center and tail base, and 0.1 seconds for all other body parts.

The arena was segmented into functionally distinct spatial zones: a 10-cm-wide wall zone along the perimeter, a 20-cm-wide intermediate ring, and a central zone (circle of diameter 40 cm). Both continuous and discrete behavioral variables were calculated based on the animal's movement and position relative to these areas. Continuous variables included: Cartesian coordinates of the body center ( $x, y$ ); absolute velocity, calculated from body center displacement and smoothed with a 0.25-second window; body direction (BD), defined as the angle from body center to head center; and head direction (HD), defined as the angle from head center to nose tip.

Discrete behavioral acts were classified based on movement dynamics. Locomotor states were defined by current speed: fast locomotion (run,  $> 5$  cm/s), slow locomotion (walk, 1–5 cm/s), and rest ( $< 1$  cm/s). Freezing was defined as simultaneous decrease of both body center velocity ( $< 1$  cm/s) and nose tip velocity ( $< 2$  cm/s). Rearing was detected by a transient reduction in the distance between the hind limbs and the tail base. Spatial zone occupancy (wall zone, center zone) was determined by the position of the body center. All discrete variables were smoothed using a 0.25-second median filter to remove noise and enforce minimal event duration.

## Processing of calcium imaging data

Calcium imaging data were processed using BEARMIND (<https://github.com/iabs-neuro/bearmind>), a custom analysis pipeline built on the CalmAn framework (*Giovannucci et al., 2019*). Preprocessing included motion correction via NoRMCorre (*Pnevmatikakis and Giovannucci, 2017*) followed by source extraction using CNMF-E (*Zhou et al., 2018*). All retained components were visually inspected to exclude artifacts and duplicates. Fluorescence traces were normalized as  $dF/F$ , and spatial maps were registered across sessions using CellReg (*Sheintuch et al., 2017*) to track individual neurons longitudinally.

In total, the dataset comprises 39 sessions from 13 animals (3 sessions per animal), with a mean of 373 simultaneously recorded neurons per session (range 26–695; 14,533 neuron-sessions total) at a frame rate of 20 Hz.

## Software engineering

DRIADA is distributed as a Python package installable via `pip install driada`. The source code is organized into six top-level modules (`intense`, `dim_reduction`, `network`, `rsa`, `information`, `recurrence`) plus supporting modules for experiment management, synthetic data generation, dimensionality estimation, and visualization. The package supports Python 3.9 through 3.13 and reads NWB (Neurodata Without Borders) files directly for interoperability with existing neurophysiology data repositories.

The test suite comprises 2000+ automated tests covering unit tests for individual functions, integration tests for multi-module workflows, and regression tests for numerical reproducibility. Continuous integration runs the full suite on every commit.

Seven tutorial notebooks (Google Colab compatible) demonstrate end-to-end workflows from data loading through selectivity testing, dimensionality reduction, and network analysis. Twenty-eight example scripts provide focused demonstrations of individual modules and cross-module integration patterns. The synthetic data generators described above serve both as validation tools and as educational examples that produce self-contained experiments without requiring real data.

Documentation is hosted at <https://driada.readthedocs.io> and includes API reference generated from docstrings, installation instructions, and usage guides.

## Acknowledgments

This work was supported by the Non-Commercial Foundation for Support of Science and Education “INTELLECT”. N.P. acknowledges support of IDEAS research center.

## Author contributions

**Nikita Pospelov:** Conceptualization, Software, Methodology, Validation, Formal analysis, Data curation, Writing — original draft, Writing — review & editing, Visualization, Project administration. **Viktor Plusnin:** Software, Validation, Data curation, Writing — review & editing. **Olga Rogozhnikova:** Software, Formal analysis, Writing — review & editing. **Anna Ivanova:** Investigation, Data curation, Writing — review & editing. **Vladimir Sotnikov:** Methodology, Investigation, Resources, Writing — review & editing. **Margarita Orobets:** Investigation, Data curation. **Ksenia Toropova:** Methodology, Validation, Investigation, Data curation, Writing — review & editing. **Olga Ivashkina:** Methodology, Validation, Investigation, Data curation, Resources, Writing — review & editing, Visualization. **Vladik Avetisov:** Formal analysis, Writing — review & editing. **Konstantin Anokhin:** Supervision, Resources, Funding acquisition, Writing — review & editing.

## Competing interests

The authors declare that no competing interests exist.

## Data availability

The full hippocampal calcium-imaging dataset—raw miniscope videos, extracted fluorescence traces, synchronized behavioral variables, and computation results—will be made publicly available upon publication of the accompanying data descriptor (*Plusnin et al., 2026*). Until then, the data are available from the authors upon reasonable request.

## Code availability

DRIADA (Dimensionality Reduction for Integrated Activity Data Analysis) is available at <https://github.com/iabs-neuro/driada> under the MIT License, with documentation at <https://driada.readthedocs.io>.

The BEARMIND pipeline for miniscope video analysis is available at <https://github.com/iabs-neuro/bearmind>.

The SPHYNX pipeline for automated behavioral analysis (*Plusnin et al., 2024*) is available at <https://github.com/iabs-neuro/sphynx>.

## Ethics

All procedures were approved by the Commission of Bioethics of Lomonosov Moscow State University (Application № 159-g, approved during Bioethics Commission meeting № 154-d-r held on 17.08.2023), and followed the Russian Federation Order N 267 MZ and the NIH Guide for the Care and Use of Laboratory Animals.

## References

- Acharya, L., Aghajan, Z. M., Vuong, C., Moore, J. J., and Mehta, M. R. (2016). Causal influence of visual cues on hippocampal directional selectivity. *Cell*, 164(1–2):197–207.
- Bandt, C. and Pompe, B. (2002). Permutation entropy: a natural complexity measure for time series. *Physical Review Letters*, 88(17):174102.
- Battiston, F., Amico, E., Barrat, A., Bianconi, G., Ferraz de Arruda, G., Franceschiello, B., Iacopini, I., Kéfi, S., Latora, V., Moreno, Y., et al. (2021). The physics of higher-order interactions in complex systems. *Nature Physics*, 17(10):1093–1098.

- Bobyleva, A., Gorsky, A., Nechaev, S., Valba, O., and Pospelov, N. (2025). Metric structural human connectomes: Localization and multifractality of eigenmodes. *Network Neuroscience*, 9(2):682–711.
- Bullmore, E. and Sporns, O. (2009). Complex brain networks: graph theoretical analysis of structural and functional systems. *Nature Reviews Neuroscience*, 10(3):186–198.
- Chung, S. and Abbott, L. F. (2021). Neural population geometry: An approach for understanding biological and artificial neural networks. *Current Opinion in Neurobiology*, 70:137–144.
- Chung, S. and Abbott, L. F. (2023). Common population codes produce extremely nonlinear neural manifolds. *Proceedings of the National Academy of Sciences*, 120(39):e2305853120.
- Climer, J. R. and Dombeck, D. A. (2021). Information theoretic approaches to deciphering the neural code with functional fluorescence imaging. *eNeuro*, 8(5):ENEURO.0266–21.2021.
- Coifman, R. R. and Lafon, S. (2006). Diffusion maps. *Applied and Computational Harmonic Analysis*, 21(1):5–30.
- Combrisson, E., Basanisi, R., Cordeiro, V. L., Ince, R. A., and Brovelli, A. (2022). Frites: A Python package for functional connectivity analysis and group-level statistics of neurophysiological data. *Journal of Open Source Software*, 7(79):3842.
- Cunningham, J. P. and Yu, B. M. (2014). Dimensionality reduction for large-scale neural recordings. *Nature Neuroscience*, 17(11):1500–1509.
- Denker, M., Yegenoglu, A., Carde, C., Gutzen, R., Peyser, A., Grün, S., Dahmen, D., Morrison, A., Diesmann, M., and Davison, A. P. (2024). Elephant—comprehensive open-source toolbox for the analysis of electrophysiological data. *Research Ideas and Outcomes*, 10:e131274.
- Donges, J. F., Heitzig, J., Beronov, B., Wiedermann, M., Runge, J., Feng, Q. Y., Tupikina, L., Stolbova, V., Donner, R. V., Marwan, N., Dijkstra, H. A., and Kurths, J. (2015). Unified functional network and nonlinear time series analysis for complex systems science: The pyunicorn package. *Chaos: An Interdisciplinary Journal of Nonlinear Science*, 25(11):113101.
- Donner, R. V., Zou, Y., Donges, J. F., Marwan, N., and Kurths, J. (2010). Recurrence networks—a novel paradigm for nonlinear time series analysis. *New Journal of Physics*, 12(3):033025.
- Dubreuil, A., Valente, A., Beiran, M., Mastrogiuseppe, F., and Ostojic, S. (2022). The role of population structure in computations through neural dynamics. *Nature Neuroscience*, 25:783–794.
- Eastwood, C. and Williams, C. K. I. (2018). A framework for the quantitative evaluation of disentangled representations. In *International Conference on Learning Representations*.
- Esparza, J., Quintanilla, J. P., Cid, E., Medeiros, A. C., Gallego, J. A., and Menendez de la Prida, L. (2025). Cell-type-specific manifold analysis discloses independent geometric transformations in the hippocampal spatial code. *Neuron*, 113(7):1098–1109.e6.
- Finkelstein, A., Derdikman, D., Rubin, A., Foerster, J. N., Las, L., and Ulanovsky, N. (2015). Three-dimensional head-direction coding in the bat brain. *Nature*, 517:159–164.
- Fusi, S., Miller, E. K., and Rigotti, M. (2016). Why neurons mix: high dimensionality for higher cognition. *Current Opinion in Neurobiology*, 37:66–74.
- Gardner, R. J., Hermansen, E., Pachitariu, M., Buber, Y., Baez-Nieto, D., Dunn, B. A., Moser, M.-B., and Moser, E. I. (2022). Toroidal topology of population activity in grid cells. *Nature*, 602:123–128.
- Geva, N., Deitch, D., Rubin, A., and Ziv, Y. (2023). Time and experience differentially affect distinct aspects of hippocampal representational drift. *Neuron*, 111(15):2357–2366.e5.
- Giovannucci, A., Friedrich, J., Gunn, P., Kalfon, J., Brown, B. L., Koay, S. A., Taxidis, J., Najafi, F., Gauthier, J. L., Zhou, P., et al. (2019). CalmAn: An open source tool for scalable calcium imaging data analysis. *eLife*, 8:e38173.
- Hubel, D. H. and Wiesel, T. N. (1962). Receptive fields, binocular interaction and functional architecture in the cat's visual cortex. *The Journal of Physiology*, 160(1):106–154.
- Ince, R. A., Giordano, B. L., Kayser, C., Rousset, G. A., Gross, J., and Schyns, P. G. (2017). A statistical framework for neuroimaging data analysis based on mutual information estimated via a Gaussian copula. *Human Brain Mapping*, 38(3):1541–1573.

- Jazayeri, M. and Ostojic, S. (2021). Interpreting neural computations by examining intrinsic and embedding dimensionality of neural activity. *Current Opinion in Neurobiology*, 70:113–120.
- Kennel, M. B., Brown, R., and Abarbanel, H. D. (1992). Determining embedding dimension for phase-space reconstruction using a geometrical construction. *Physical Review A*, 45(6):3403.
- Kobak, D., Brendel, W., Constantinidis, C., Feierstein, C. E., Kepecs, A., Mainen, Z. F., Qi, X.-L., Romo, R., Uchida, N., and Machens, C. K. (2016). Demixed principal component analysis of neural population data. *eLife*, 5:e10989.
- Koh, T. H., Bishop, W. E., Kawashima, T., Jeon, B. B., Srinivasan, R., Mu, Y., Ahrens, M. B., Chase, S. M., Yu, B. M., Bhashyam, S. V., and Bhalla, U. S. (2023). Dimensionality reduction of calcium-imaged neuronal population activity. *Nature Computational Science*, 3(1):71–85.
- Kononov, R. A., Pospelov, N. A., Anokhin, K. V., Nekorkin, V. V., and Maslennikov, O. V. (2025). Emergence of hybrid computational dynamics through reinforcement learning. *arXiv preprint arXiv:2510.11162*.
- Kraskov, A., Stögbauer, H., and Grassberger, P. (2004). Estimating mutual information. *Physical Review E*, 69(6):066138.
- Kriegeskorte, N., Mur, M., and Bandettini, P. A. (2008). Representational similarity analysis—connecting the branches of systems neuroscience. *Frontiers in Systems Neuroscience*, 2:4.
- Lacasa, L., Luque, B., Ballesteros, F., Luque, J., and Nuno, J. C. (2008). From time series to complex networks: The visibility graph. *Proceedings of the National Academy of Sciences*, 105(13):4972–4975.
- Leutgeb, S., Ragozzino, K. E., and Mizumori, S. J. (2000). Convergence of head direction and place information in the CA1 region of hippocampus. *Neuroscience*, 100(1):11–19.
- Lorenz, G. M., Engel, N. M., Celotto, M., Koçillari, L., Curreli, S., Fellin, T., and Panzeri, S. (2025). MINT: A toolbox for the analysis of multivariate neural information coding and transmission. *PLOS Computational Biology*, 21(1):e1012934.
- Luque, B., Lacasa, L., Ballesteros, F., and Luque, J. (2009). Horizontal visibility graphs: Exact results for random time series. *Physical Review E*, 80:046103.
- Maffulli, R., Casal, M. A., Celotto, M., Zucca, S., Safaai, H., Fellin, T., and Panzeri, S. (2022). NIT: an open-source tool for information theoretic analysis of neural population data. *bioRxiv*.
- Manley, J., Lu, S., Barber, K., Demas, J., Kim, H., Meyer, D., Martínez Traub, F., and Vaziri, A. (2024). Simultaneous, cortex-wide dynamics of up to 1 million neurons reveal unbounded scaling of dimensionality with neuron number. *Neuron*, 112(10):1694–1709.e5.
- Marwan, N., Carmen Romano, M., Thiel, M., and Kurths, J. (2007). Recurrence plots for the analysis of complex systems. *Physics Reports*, 438(5–6):237–329.
- Mathis, A., Mamidanna, P., Cury, K. M., Abe, T., Murthy, V. N., Mathis, M. W., and Bethge, M. (2018). DeepLabCut: markerless pose estimation of user-defined body parts with deep learning. *Nature Neuroscience*, 21(9):1281–1289.
- McCullough, M., Small, M., Stemler, T., and Lu, H. H.-C. (2015). Time lagged ordinal partition networks for capturing dynamics of continuous dynamical systems. *Chaos*, 25:053101.
- McInnes, L., Healy, J., Saul, N., and Grossberger, L. (2018). UMAP: Uniform manifold approximation and projection. *Journal of Open Source Software*, 3(29):861.
- Munn, B. R., Müller, E. J., Wainstein, G., Zamani Esfahlani, F., Shinohara, R. T., Betzel, R. F., Power, J. D., and Bhatt, D. (2024). Multiscale organization of neuronal activity unifies scale-dependent theories of brain function. *Cell*.
- Neri, M., Vinchhi, D., Ferreyra, C., Robiglio, T., Ates, O., Ontivero-Ortega, M., Brovelli, A., Marinazzo, D., and Combrisson, E. (2024). HOI: A Python toolbox for high-performance estimation of Higher-Order Interactions from multivariate data. *Journal of Open Source Software*, 9(103):7360.
- O’Keefe, J. and Dostrovsky, J. (1971). The hippocampus as a spatial map: Preliminary evidence from unit activity in the freely-moving rat. *Brain Research*, 34(1):171–175.
- Paxinos, G. and Franklin, K. B. J. (2019). *Paxinos and Franklin’s the Mouse Brain in Stereotaxic Coordinates*. Academic Press, 5th edition.

- Plusnin, V., Ivashkina, O., Pospelov, N., Rogozhnikova, O., Savelev, N., Sotskov, V., Toropova, K., and Anokhin, K. (2024). Sphynx: An automated behavioral analysis tool for neuronal selectivity identification. In *2024 Sixth International Conference Neurotechnologies and Neurointerfaces (CNN)*, pages 156–159. IEEE.
- Plusnin, V., Pospelov, N., Ivanova, A., Orobets, M., Rogozhnikova, O., Savelev, N., Sotskov, V., Toropova, K., Ivashkina, O., and Anokhin, K. (2026). Mouse hippocampal one-photon calcium imaging dataset during free exploration tasks. In preparation.
- Pnevmatikakis, E. A. and Giovannucci, A. (2017). NoRMCorre: An online algorithm for piecewise rigid motion correction of calcium imaging data. *Journal of Neuroscience Methods*, 291:83–94.
- Pospelov, N., Levchenko, E., Tiselko, V., Safronova, R., Zakharov, I., Sotskov, V., and Anokhin, K. (2022). Network entropy analysis reveals high heterogeneity of human functional networks. In *2022 6th Scientific School Dynamics of Complex Networks and their Applications (DCNA)*, pages 196–199.
- Pospelov, N., Rogozhnikova, O., Plusnin, V., Ivanova, A., Toropova, K., Ivashkina, O., and Anokhin, K. (2024). Effective dimensionality of neuronal population activity in hippocampus correlates with behavior. In *2024 8th Scientific School Dynamics of Complex Networks and their Applications (DCNA)*, pages 196–199.
- Pospelov, N., Teterova, A., Martynova, O., and Anokhin, K. (2021). The laplacian eigenmaps dimensionality reduction of fMRI data for discovering stimulus-induced changes in the resting-state brain activity. *NeuroImage: Reports*, 1(3):100035.
- Pospelov, N. A., Plusnin, V. V., Rogozhnikova, O., Ivanova, A., Sotskov, V. P., Toropova, K., Ivashkina, O., and Anokhin, K. V. (2026). INTENSE: Information-theoretic neuron-feature selectivity testing for calcium imaging. *arXiv preprint arXiv:2603.04622*.
- Rigotti, M., Barak, O., Warden, M. R., Wang, X.-J., Daw, N. D., Miller, E. K., and Fusi, S. (2013). The importance of mixed selectivity in complex cognitive tasks. *Nature*, 497(7451):585–590.
- Rubinov, M. and Sporns, O. (2010). Complex network measures of brain connectivity: uses and interpretations. *NeuroImage*, 52(3):1059–1069.
- Saxena, S. and Cunningham, J. P. (2019). Towards the neural population doctrine. *Current Opinion in Neurobiology*, 55:103–111.
- Schneider, S., Lee, J. H., and Mathis, M. W. (2023). Learnable latent embeddings for joint behavioural and neural analysis. *Nature*, 617(7960):360–368.
- Sheintuch, L., Rubin, A., Brande-Eilat, N., Geva, N., Sadeh, N., Pinchasof, O., and Ziv, Y. (2017). Tracking the same neurons across multiple days in Ca<sup>2+</sup> imaging data. *Cell Reports*, 21(4):1102–1115.
- Sotskov, V. P., Pospelov, N. A., Plusnin, V. V., and Anokhin, K. V. (2022). Calcium imaging reveals fast tuning dynamics of hippocampal place cells and CA1 population activity during free exploration task in mice. *International Journal of Molecular Sciences*, 23(2):638.
- Sporns, O., Tononi, G., and Kötter, R. (2005). The human connectome: A structural description of the human brain. *PLoS Computational Biology*, 1(4):e42.
- Stringer, C., Pachitariu, M., Steinmetz, N., Carandini, M., and Harris, K. D. (2019). High-dimensional geometry of population responses in visual cortex. *Nature*, 571(7765):361–365.
- Sulaimany, S. and Safahi, A. (2023). Visibility graph analysis for brain: scoping review. *Frontiers in Neuroscience*, 17:1268485.
- Taube, J. S. (1995). Head direction cells recorded in the anterior thalamic nuclei of freely moving rats. *Journal of Neuroscience*, 15(1 Pt 1):70–86.
- Taube, J. S., Muller, R. U., and Ranck, J. B. J. (1990). Head-direction cells recorded from the postsubiculum in freely moving rats. i. description and quantitative analysis. *Journal of Neuroscience*, 10(2):420–435.
- Tye, K. M., Miller, E. K., Taschbach, F. H., Benna, M. K., Rigotti, M., and Fusi, S. (2024). Mixed selectivity: Cellular computations for complexity. *Neuron*, 112(13):2049–2067.
- Vaccari, F. E., Diomedì, S., Filippini, M., Hadjimitsakakis, K., and Fattori, P. (2022). New insights on single-neuron selectivity in the era of population-level approaches. *Frontiers in Integrative Neuroscience*, 16:929052.

- Varley, T. F. and Sporns, O. (2022). Network analysis of time series: Novel approaches to network neuroscience. *Frontiers in Neuroscience*, 15:787068.
- Venna, J. and Kaski, S. (2006). Local multidimensional scaling. *Neural Networks*, 19:889–899.
- Viejo, G., Cacucci, F., Bhatt, D., de la Cuesta-Zuluaga, J., Bhaskaran, M., and Brandon, M. P. (2023). Pynapple, a toolbox for data analysis in neuroscience. *eLife*, 12:RP85786.
- Vyas, S., Golub, M. D., Sussillo, D., and Shenoy, K. V. (2020). Computation through neural population dynamics. *Annual Review of Neuroscience*, 43:249–275.
- Williams, P. L. and Beer, R. D. (2010). Nonnegative decomposition of multivariate information. *arXiv preprint arXiv:1004.2515*.
- Wollstadt, P., Lizier, J. T., Vicente, R., Finn, C., Martinez-Zarzuela, M., Mediano, P., Novelli, L., and Wibral, M. (2019). IDTxI: The Information Dynamics Toolkit xl: a Python package for the efficient analysis of multivariate information dynamics in networks. *Journal of Open Source Software*, 4(34):1081.
- Zhou, P., Resendez, S. L., Rodriguez-Romaguera, J., Jimenez, J. C., Neufeld, S. Q., Giovannucci, A., Friedrich, J., Pnevmatikakis, E. A., Stuber, G. D., Hen, R., Kheirbek, M. A., Sabatini, B. L., Kass, R. E., and Paninski, L. (2018). Efficient and accurate extraction of in vivo calcium signals from microendoscopic video data. *eLife*, 7:e28728.
- Ziv, Y., Burns, L. D., Cocker, E. D., Hamel, E. O., Ghosh, K. K., Kitch, L. J., El Gamal, A., and Schnitzer, M. J. (2013). Long-term dynamics of CA1 hippocampal place codes. *Nature Neuroscience*, 16(3):264–266.